Research Square

Preprints are preliminary reports that have not undergone peer review.
They should not be considered conclusive, used to inform clinical practice,
or referenced by the media as validated information.

Disruption of lysine biosynthesis modulates DNA methylation and developmental programs in Arabidopsis thaliana

Wagner Araujo

wlaraujo@ufv.br

Universidade Federal de Viçosa https://orcid.org/0000-0002-4796-2616

Débora Gouveia

Universidade Federal de Viçosa

Samantha Flachbart

Heinrich-Heine University Düsseldorf

Wesley Barrios

Universidade Federal de Viçosa

Philipp Westhoff

Heinrich Heine University https://orcid.org/0000-0002-3494-9420

Pedro Reis

Universidade Federal de Viçosa

Alisdair Fernie

MPI of Molecular Plant Physiology https://orcid.org/0000-0001-9000-335X

Adriano Nunes-Nesi

Universidade Federal de Viçosa

Andreas Weber

Heinrich-Heine-University https://orcid.org/0000-0003-0970-4672

Article

Keywords: Lysine biosynthesis, L,L-diaminopimelate aminotransferase, flowering time, shoot branching, DNA methylation

Posted Date: June 29th, 2026

DOI: https://doi.org/10.21203/rs.3.rs-10021158/v1

License: This work is licensed under a Creative Commons Attribution 4.0 International License.
Read Full License

Additional Declarations: There is **NO** Competing Interest.

Abstract

Lysine metabolism is a central determinant of plant growth, coupling amino acid biosynthesis to mitochondrial electron transport and the tricarboxylic acid (TCA) cycle to sustain cellular energy homeostasis. However, whether perturbation of lysine biosynthesis reshapes developmental transitions through epigenetic regulatory pathways remains unknown. Here, we show that reduced activity of *L,L*-diaminopimelate aminotransferase (DAPAT), a key enzyme in lysine biosynthesis, markedly reprograms growth and developmental timing in *Arabidopsis thaliana*. The lysine biosynthesis-deficient mutant *dapat* exhibits severe development constraints, displaying a pronounced flowering delay under long-day conditions accompanied by reduced shoot branching, fewer siliques, lower seed number per silique, decreased seed biomass, and reduced leaf production, a comprehensive developmental phenotype that underscores the critical role of lysine metabolism in orchestrating plant growth. Strikingly, neutral-day conditions partially rescue the flowering delay in *dapat* plants, revealing an unexpected environmental plasticity that positions lysine biosynthesis at the intersection of metabolic regulation, epigenetic remodeling, and developmental timing. Gene expression analysis of key flowering-time regulators that control the photoperiodic and vernalization pathways in *Arabidopsis* revealed upregulation of CONSTANS (*CO*) and FLOWERING LOCUS C (*FLC*), downregulation of FRIGIDA (*FRI*), and unaltered FLOWERING LOCUS T (*FT*), suggesting that lysine deficiency modulates flowering through a *CO*/*FLC*-dependent regulatory framework. Using whole-genome bisulfite sequencing (WGBS) we identified 957 genes with altered methylation patterns across the plant's five chromosomes. These changes occurred in three different DNA sequence contexts: 749 genes showed differences in CpG sites, while 104 genes each showed changes in CHG and CHH contexts. These epigenetic changes coincide with altered expression of genes involved in *S*-adenosyl-methionine metabolism and chromatin regulation, including upregulation of *S*-adenosyl-methionine synthase 2 (*MAT2*), *S*-adenosyl-methionine synthase 4 (*MAT4*), and histone methyltransferase SU(VAR)3–9 HOMOLOG 4 (*SUVH4*), whereas *SUVH5* is downregulated and *SUVH6* remains unchanged. These findings uncover a previously unrecognized role for lysine biosynthesis via DAPAT enzyme in coordinating plant growth, flowering time, and reproductive output through metabolic-epigenetic regulation.

1. Introduction

Plants are sessile organisms that have evolved highly plastic developmental strategies to cope with environmental variability. Among these processes, the floral transition represents a critical developmental switch governed by complex genetic and epigenetic networks that synchronize internal metabolic status with external cues (Hemenway & Gehring, 2023; Li et al., 2025). The photoperiodic pathway, which controls plant responses to day length, is one of the most important pathways regulating flowering (Wang & Chen *et al*., 2024). In *Arabidopsis thaliana*, the transition from vegetative to the reproductive phase is orchestrated by photoperiod-dependent activation of *CONSTANS* (*CO*) and *FLOWERING LOCUS T* (*FT*). *CO*, hub in the photoperiodic regulatory network, operates as the principal transcriptional activator of the florigen gene *FT* in leaves, and its expression is strongly gated by the circadian clock. Circadian timing of *CO* transcription provides the molecular measure for day-length

detection: under short-day photoperiods, the *CO* mRNA peak falls in darkness, leading to rapid turnover, whereas under long-day conditions, the peak coincides with the light phase, stabilizing *CO* and enabling *FT* induction, thereby accelerating floral transition (Imaizumi, 2009; de Los Reyes et al., 2024; Wang & Chen *et al*., 2024).

The floral transition triggers a fundamental reprogramming of axillary meristem activity, converting the developmental fate of suppressed vegetative buds to promote the coordinated emergence of rosette and cauline branches, thus coupling flowering time control with branching architecture to optimize reproductive establishment (Schmitz & Theres, 2005; Wang & Jiao, 2018; Luo et al., 2021). Shoot branching in flowering plants, a major component of shoot architecture, is highly plastic and responsive to both genetic background and environmental factors such as phytohormones (Davis, 2009; Müller & Leyser, 2011; Gallavotti *et al*., 2013; Brewer et al., 2015; Xiaoxiao *et al*., 2023), light conditions (Finlayson *et al*., 2014; Fichtner et al., 2022), and metabolic status (Wahl et al., 2013; Mason et al., 2014; de Jong et al., 2019; Göbel & Fichtner, 2023).

In plants, lysine is synthesized via the aspartate-derived diaminopimelate (DAP) pathway, in which *L,L*-diaminopimelate aminotransferase (DAPAT; EC 2.6.1.83) catalyzes a critical transamination reaction (Azevedo et al., 2006; Song et al., 2004; Hudson et al., 2006). Loss-of-function mutation in DAPAT reduces enzyme activity by approximately 90%, resulting in a sustained pre-stress metabolic state that disrupts growth and development in the *dapat* mutant (Cavalcanti et al., 2018; Neves et al., 2024; Gouveia *et al*., 2026), thereby underscoring the central role of lysine in energy metabolism (Araújo et al., 2010, 2011; Hildebrandt, 2018; Yang et al., 2020). In plants, one of the lysine catabolic routes is the branched saccharopine pathway (SACPATH), which converts lysine to acetyl-CoA, and subsequently to 2-oxoglutarate (2-OG) via the tricarboxylic acid (TCA) cycle, where it undergoes transamination to glutamate (Moller, 1976; Arruda & Barreto, 2020). Notably, the identification of a D-2-hydroxyglutarate dehydrogenase (D2HGDH; EC 1.1.99.39)–dependent bypass that directly generates 2-OG (Engqvist et al., 2009; Araújo et al., 2010) highlights a tight integration between lysine metabolism, the TCA cycle, and the alternative respiratory pathway (for a review, *please see* Araújo et al., 2011). Both D2HGDH-mediated alternative route and the classical SACPATH pathway channel electrons into the ETF–ETFQO system, which acts as a crucial electron source for ATP synthesis in plant mitochondria (Araújo et al., 2011; Hildebrandt et al., 2015).

It is well established that lysine metabolism is closely associated with the modulation of plant growth and development (Cavalcanti et al., 2018). It has been previously demonstrated that crossing transgenic lines constitutively expressing bacterial 35S-DHPS with an At-*LKR/SDH* knockout mutant triggers progeny with abnormal reproductive phenotypes (Zhu & Galili, 2004), underscoring the critical role of LKR (EC 1.5.1.8)/ SDH (EC 1.5.1.9), the bifunctional enzyme catalyzing the first two steps of lysine catabolism via SACPATH, in maintaining lysine homeostasis and normal development. Remarkably, a distinct branch of the SACPATH is responsible for funneling carbon and nitrogen into *S*-adenosylmethionine (SAM)-dependent methylation reactions (Rébeillé et al., 2006; Amir, 2010; Hildebrandt et al., 2015). Through this route, lysine catabolism generates intermediates that contribute

to the methionine cycle, thereby supplying SAM, the universal methyl donor required for DNA, RNA, protein, lipids, hormones and secondary metabolite methylation (Fontecave et al., 2004). This metabolic connection positions lysine catabolism as a direct link between amino acid homeostasis and epigenetic regulation, with implications for chromatin organization, gene expression, and developmental transitions such as flowering time control. In summary, methionine is adenylated by one of four *S*-adenosylmethionine synthases (MATs 1–4; EC 2.5.1.6) to form SAM (Sekula *et al*., 2020), the methyl donor to histone H3 methyltransferases such as SET domain-containing group 8 (SDG8; EC 2.1.1.359), which deposits H3K36me2/3 and H3K9me2 marks (Le et al., 2025). In *sdg8* mutants, loss of these methylation marks results in de-repressed axillary meristems and a higher branching phenotype (Dong et al., 2008), highlighting that lysine-derived SAM incorporation into chromatin represents a vital epigenetic mechanism likely governing shoot branching architecture.

Here, by integrating lysine biosynthesis deficiency, flowering-time control, and genome-wide methylome remodeling, this study establishes a novel metabolic-epigenetic axis: DAPAT deficiency rewires the floral transition and shoot architecture to balance vegetative growth with reproductive output in *Arabidopsis thaliana*.

2. Results

Restriction fragment profiling reveals DAPAT site disruption

Since the loss of the DAPAT gene (AT4G33680), which encodes the third enzyme in lysine biosynthesis *L,L*-diaminopimelate aminotransferase (DAPAT; EC 2.6.1.83), is embryo lethal (Rate & Greenberg, 2001), we used an EMS-derived knockdown mutant carrying a P398S substitution in DAPAT. This mutation reduces enzyme activity by approximately 90% (Song et al., 2004; Cavalcanti et al., 2018; Gouveia *et al*., 2026).

Genotyping of the *dapat* mutant line was performed by PCR–RFLP (Zhang et al., 2005) for the first time. Genomic DNA from wild-type (WT) and *dapat* plants was amplified with primers (Extended Data Table 1) flanking the *Hha*I restriction site within the *DAPAT* gene, yielding an undigested product of 1,219 bp (Extended Data Fig. 1). Following *Hha*I digestion, WT DNA (lane 2) was cleaved at two internal *HhaI* sites, producing four fragments of 647 bp, 263 bp, 233 bp, and 76 bp. In contrast, *dapat* mutant DNA (lanes 3–9) lacked the primary *Hha*I recognition site due to the point mutation; thus, digestion yields only three fragments: an uncut 910 bp fragment (combining the two segments that would be separated in WT) and the downstream 233 bp and 76 bp fragments. This pattern confirms that the DAPAT mutation leads to a specific nucleotide substitution, abolishing the *Hha*I site and distinguishing it from the WT allele.

Complementation lines expressing DAPAT under the constitutive UBQ10 promoter in the pUTKAN-HA construct (Krebs *et al*., 2012) fully restored normal growth under control conditions (Extended Data Fig. 1b), confirming that the growth inhibition phenotype of *dapat* mutants results directly from loss of DAPAT activity.

Impaired vegetative growth and flowering time in dapat plants

Given the marked growth and developmental defects triggered by the DAPAT mutation (Song et al., 2004; Cavalcanti et al., 2018; Neves et al., 2024; Gouveia *et al*., 2026), we investigated its unexplored impact on the juvenile-to-reproductive phase transition. Under a 16-h light (long-days, LD) photoperiod, *dapat* plants showed marked growth inhibition, delayed inflorescence emergence and altered reproductive architecture (Figs. 1–2). To further characterize reproductive performance and seed phenotype, we quantified silique number per plant, seeds per silique and silique dimensions, including length and width (Fig. 1c–f). The disruption of DAPAT activity in the mutant markedly diminished silique production (Fig. 1c) and seed yield per silique (Fig. 1d). By contrast, only minor differences in silique dimensions were observed between genotypes.

To determine the extent of reproductive constraints in *dapat* plants, we cultivated a larger population per genotype under LD conditions and quantified their shoot branching patterns (Fig. 2). Unlike WT, the *dapat* mutants exhibited a markedly altered branching: strongly reduced primary rosette (R1; Fig. 2b) and cauline primary branches (C1; Fig. 2d) per plant, with secondary rosette (R2; Fig. 2c) and cauline secondary branches (C2; Fig. 2e) unaffected. Altogether, our results indicate that disruption of DAPAT activity alters *Arabidopsis* shoot architecture, favoring lateral branch formation at the expense of primary shoot initiation.

DAPAT mutation impairs both vegetative and reproductive leaf development

Quantitative analysis of leaf development revealed a reduction in rosette leaf number (RL; Fig. 2f), cauline leaf number (CL; Fig. 2g) and total leaf number (rosette plus cauline; Fig. 2h) in *dapat*. A similar pattern was observed under a 12-h light (neutral-days, ND) photoperiod (Extended Data Fig. 2), where the DAPAT mutation also reduced rosette leaf number and total leaf number in (Extended Data Fig. 2g–i). Fichtner et al. (2022) quantified rosette-node branching in *A. thaliana* using two primary metrics: R_1, defined as the number of primary rosette branches (*i.e*., axillary shoots emerging from rosette leaf axils), and RL, the number of rosette leaves (each leaf subtends a potential branch node), with the R_1/RL ratio calculation defined as the number of primary rosette branches (R_1)/´divided by the number of rosette leaves (RL). Since total number of rosette leaves (RL) can vary with flowering time or growth conditions, dividing R_1 by RL normalizes branch counts relative to the number of available leaf axils. This approach allows for correction of differences in rosette leaf production that accompany altered flowering time or environmental influences, revealing true alterations in branching propensity per available node, independent of total leaf count. In our analysis, *dapat* plants grown under LD conditions exhibited a reduced R_1/RL ratio compared with WT (Fig. 2i). Conversely, *dapat* grown under ND showed an increased R_1/RL ratio, indicating an opposite behavior (Extended Data Fig. 2j). These findings highlight the impact of DAPAT disruption on leaf development and shoot branching, underscoring its essential role in regulating foliar growth across different environmental conditions.

DAPAT mutation reveal shifted timing and frequency of bolting

Building on these observations, we accessed the temporal extent of the flowering delay caused by the DAPAT mutation. *dapat* plants showed substantial bolting delays under both LD (Fig. 3a) and ND (Fig. 3c) conditions. Under LD, WT plants began bolting on day 0, with a peak at days 5–7, whereas bolting in the *dapat* mutant started later, peaked at days 8–10, and occurred at a lower overall frequency. Under ND, *dapat* still exhibited a delayed floral transition, with bolting beginning at day 8 compared with day 0 in WT, but the peak occurred earlier in *dapat* (around day 10) than in WT (around day 14). Quantitative analysis of primary rosette branch accumulation over time further reveals photoperiod-specific differences. Under LD, WT plants rapidly accumulated ~ 7 bolting stems per replicate by day 12, whereas *dapat* reached only ~ 5 stems in the same period (Fig. 3b). Photoperiod switching markedly altered emergence patterns: both genotypes initiate branching simultaneously around day 8 under ND, but *dapat* mutant accumulated more bolting stems overall (Fig. 3d). These findings suggest that DAPAT impairment induces photoperiod-dependent reprogramming of the flowering transition, with *dapat* plants exhibiting delayed initiation but accelerated peak bolting under ND, revealing a complex metabolic modulation of phase change dynamics.

dapat mutant seeds exhibits alters phenotype and storage compounds

Extending our observation that lysine biosynthesis disruption affects flowering, reproductive output and silique phenotype, we asked whether these constraints arise before seedling establishment, at the level of seed reserves. In line with Cavalcanti et al. (2018), we confirmed that disruption of lysine biosynthesis delays germination, increasing T_{50} from 41 h 58 min in WT to 53 h 05 min in *dapat* (Extended Data Fig. 3a,b). At the level of seed reserves, seed trait analysis revealed that *dapat* seeds exhibit significantly reduced weight (Extended Data Fig. 3c), despite markedly elevated total protein content (Extended Data Fig. 3d).

Following DAPAT's impact on germination dynamics and seed protein content, we assessed carbon, nitrogen, and isotopic composition, in parallel with the fatty acid methyl ester (FAMEs) profiles. The isotopic composition remained unchanged (Extended Data Fig. 3h-k), indicating stable carbon allocation in the mutant. By contrast, FAMEs profiles of C14–C18 species in dry seeds revealed clear genotype-specific differences (Extended Data Fig. 3e). As expected, C14:0 was essentially absent in both WT and *dapat*. However, palmitic acid (16:0) abundance decreased from approximately 0.38 in WT to ~ 0.35 in *dapat* (p = 0.019), and stearic acid (18:0) similarly declined from ~ 0.15 to ~ 0.13 in the mutant (p = 0.006). The predominant oleic acid isomer (18:1_a) decreased from ~ 0.22 in WT to ~ 0.19 in *dapat* (p = 0.006), while the minor isomer (18:1_b) declined from ~ 0.008 to ~ 0.005 (p = 0.012). The most pronounced reduction was observed in linoleic acid (18:2_a), which declined from approximately 0.55 in WT to ~ 0.45 in *dapat* (p = 0.004). By contrast, α-linolenic acid (18:3_a) showed only a slight, non-significant decrease in the mutant (~ 0.54 vs. ~0.60; p = 0.090). The relative abundance of C20–C22 FAMEs was substantially lower in *dapat* seeds (Extended Data Fig. 3f). Specifically, 20:0 levels decreased from approximately 0.085 in WT to 0.065 in *dapat* (p = 0.004), 20:1_a dropped from around 0.255 to 0.205 (p = 0.007), and 20:2 declined from about 0.215 to 0.185 (p = 0.007). By contrast, the reduction in 20:1_b did not reach statistical significance (p = 0.061), and the levels of 22:0 and 22:1 remained

essentially unchanged ($p = 0.152$ and $p = 0.957$, respectively). Together, these data indicate that DAPAT-dependent lysine biosynthesis is required not only for normal germination, but also for proper reserve composition and seed quality, supporting the idea that developmental constraints are already established before seedling emergence.

Lysine biosynthesis disruption reprograms flowering-time regulators and SAM-dependent epigenetic pathways

Our next question prompted us to investigate whether lysine biosynthesis disruption affects the expression of flowering-time regulators. Transcript analysis of genes associated with phase transition revealed that reduced DAPAT activity substantially alters the expression of key flowering-time genes (Fig. 4a,b). Notably, *CONSTANS* (*CO*) transcript levels increased more than three folds in the *dapat* mutant compared with WT (Fig. 4a), whereas *FLOWERING LOCUS C* (*FLC*) was strongly upregulated in the mutant, showing an approximately 28-fold increase ($p < 0.001$) (Fig. 4b). By contrast, *FRIGIDA* (*FRI*) expression was reduced by ~ 40% in the *dapat* mutant ($p < 0.05$), while *FLOWERING LOCUS T* (*FT*) transcript levels remained unchanged between genotypes (Fig. 4a). Together, these shifts suggest that DAPAT deficiency leads to a *CO*- and *FLC*-dependent delay in floral induction.

Following differential expression analysis of *CO*, *FRI*, and *FLC* in *dapat* plants, we examined methyltransferas (MTases)-encoding genes, specifically the genes encoding *S*-adenosylmethionine (SAM) synthases, to assess how perturbation of the aspartate-derived pathway linking lysine and methionine biosynthesis may affect SAM-dependent epigenetic regulation of flowering time. Remarkably, transcript levels of the *MAT2* and *MAT4* were significantly elevated by approximately 20–30% in *dapat* plants (Fig. 4c), suggesting that the mutant plants may activate a feedback mechanism to enhance SAM biosynthesis or recycling.

In light of the induction of *MAT2* and *MAT4*, two major determinants of *S*-adenosylmethionine (SAM) synthesis, we next examined the expression of the *SUPPRESSOR OF VARIEGATION 3–9 HOMOLOG (SUVH)* family, a group of plant-specific histone H3K9 MTases that deposit repressive marks and are central to chromatin organization and transcriptional regulation. This analysis was essential to better understand how shifts in methyl-donor availability may influence histone methylation dynamics and, consequently, the epigenetic control of developmental transitions. Transcript levels revealed that *dapat* plants exhibit differential regulation of three *SUVHs* genes compared with WT (Fig. 5d). *SUVH4* transcript levels were significantly elevated in the *dapat* mutant, whereas *SUVH5* expression was markedly reduced. *SUVH6* levels did not differ significantly between genotypes. Together, these results indicate that the DAPAT mutation selectively upregulates *SUVH4* and represses *SUVH5*, while leaving *SUVH6* expression largely unchanged under the tested growth conditions.

Lysine biosynthesis impairment reshapes differential methylated genes (DMGs) distribution across genic and intergenic regions

Guided by the differential expression of *MATs* and *SUVHs* families, we performed bisulfite sequencing in WT and *dapat* plants using the same pre-bolting sampling strategy (ND growth; Extended Data Fig. 4) to evaluate how perturbation of lysine biosynthesis affects genome-wide DNA methylation patterns and epigenetic regulation of developmental transitions. This analysis revealed 749 CpG differentially methylated genes (DMGs) in *dapat* (490 retained with a 20% cutoff), with hierarchical clustering delineating hyper- and hypomethylated clusters (genes with increased or decreased methylation, respectively; Fig. 5). CHG (H denotes A, T, or C nucleotides) and CHH-context analyses revealed 104 CHG DMGs and only 6 CHH DMGs retained after 20% cutoff, similarly, segregated into hyper- and hypomethylated groups by clustering (Fig. 5a-c).

DMGs in the *dapat* mutant were detected across distal intergenic, promoter, exon, 3'UTR and downstream segments (Extended Data Table 3). CpG DMGs favored hypermethylation in gene bodies and promoters, while CHG and CHH showed balanced hypo/hyper patterns in intergenic regions. In the CpG context, 34 DMGs mapped to exons, of which 19 were hypomethylated and 15 hypermethylated, whereas only one hypomethylated exon DMR was detected in the CHG context. Distal intergenic regions harbored four CpG DMGs (one hypo- and three hypermethylated), three CHG DMGs (one hypo- and two hypermethylated) and a single hypermethylated CHH DMR. The 3'UTR contained 20 CpG DMGs (15 hypomethylated and five hypermethylated) and two CHG DMGs (one hypo- and one hypermethylated). Finally, downstream regions displayed three hypomethylated CpG DMGs and two CHG DMGs (one hypo- and one hypermethylated). Together, these patterns indicate that DAPAT activity deficiency triggers genome-wide epigenetic reprogramming across CpG, CHG and CHH sites, that preferentially remodel CpG methylation within gene bodies and regulatory regions, with more modest changes in non-CpG contexts.

The Gene Ontology (GO) analysis revels the top 15 biological processes DMGs across CpG, CHG, and CHH sites. Pathway enrichment of associated genes highlighted morphogenesis, developmental growth and cytoskeleton organization (Fig. 6a). Analysis of DNA methylation differences between WT and *dapat* samples across genes associated with three GO terms related to cell growth and morphogenesis (GO:0009826, GO:0000902, GO:0060560) revealed a coherent epigenomic signature (Fig. 6b-d). The dominant feature was pronounced CpG hypomethylation (− 20% to − 55%) concentrated at promoter and exonic regions of a shared gene core comprising *BRI1*, *FEI1*, *ANX2*, *COBL7*, *RIC5*, *PAS1*, *XRN4* and *NMNAT*. In contrast, two loci displayed atypical CpG hypermethylation: *WAK2* (~ + 26%) and AT4G17810 (~ + 45%). A more extreme case was observed at AT3G01015, which showed simultaneous hypermethylation across all three sequence contexts at distal intergenic regions (CpG ~ + 5%, CHG ~ + 49%, CHH ~ + 26%). Across the remaining loci, CHG and CHH methylation levels remained broadly stable, ranging between − 20% and + 20%.

Finally, a striking enriched pathway linked to the DAPAT phenotype is the response to nitrogenous compounds (Fig. 6d), featuring nine genes with differentially methylated genes, predominantly CG-context promoter DMGs for *XRN4* (AT1G54490), *CYT1* (cytokinesis-defective 1), *CRT1a* (calreticulin 1a, AT1G56340), *BIP2* (heat shock 70 kDa protein, AT5G42020) and *MNS1* (mannosyl-oligosaccharide 1,2-α-

mannosidase, AT1G51590), alongside CHG-site DMGs for *ATL9* (RING zinc-finger E3 ubiquitin ligase, AT2G35000). An additional 11 enriched biological processes associated with DMGs across CpG, CHG, and CHH contexts are presented in Extended Data Figs. 6 and 7. Genotype accounted for most of the variance among differentially methylated cytosines across all three sites, as shown by principal component analyses (Extended Data Fig. 8a–c). These results reveal a selective methylation signature in *dapat* plants, predominantly driven by CpG remodeling at regulatory regions of genes associated with morphogenesis, growth, and nitrogen-responsive pathways. Rather than indicating a global disruption of DNA methylation, this pattern supports targeted epigenetic reprogramming of developmental modules that may underlie the DAPAT phenotype.

3. Discussion

Lysine deficiency from DAPAT disruption delays phase transition and reprograms branching patterns

Disruption of lysine biosynthesis at the *L,L*-diaminopimelate aminotransferase (DAPAT) step, which reduces enzyme activity by approximately 90% (Hudson et al., 2006), induces a constitutive pre-stress metabolic state that impairs vegetative growth even under optimal conditions (Song et al., 2004; Cavalcanti et al., 2018; Neves et al., 2024; Gouveia *et al*., 2026). Given that alterations in lysine levels can compromise seed germination rates and yield in plants (Angelovici et al., 2011; Wong *et al*., 2014; Cavalcanti et al., 2018), we asked whether impaired lysine biosynthesis in *dapat* plants also affects seed storage composition, potentially revealing a developmental constraint that begins before seedling establishment.

At the level of seed reserves, seed trait analysis revealed that *dapat* seeds exhibit significantly reduced weight (Extended Data Fig. 3c), despite markedly elevated total protein content (Extended Data Fig. 3d). The fatty acid methyl esters (FAMEs) profile revealed extensive depletion of major and very-long-chain fatty acids in dry *dapat* mutant seeds (Extended Data Fig. 3e,f). This included complete absence of C14:0 (Extended Data Fig. 3e), alongside a near absence of C20 fatty acids (Extended Data Fig. 3f), pointing to a targeted disruption of very-long-chain fatty acid synthesis and accumulation. The selective depletion of C20 species indicates impaired triacylglycerol assembly rather than enhanced catabolism. As very-long-chain C20 fatty acids are key triacylglycerol constituents, their loss, together with reduced C16–C18 FAMEs, suggests that the DAPAT impairment specifically disrupts fatty acid elongation and incorporation into storage lipids (Bernhardt *et al*., 2011), without altering overall seed elemental composition (Extended Data Fig. 3h-k). Together, these findings suggest that DAPAT mutation imposes a developmental constraint that begins during seed formation and carries over into vegetative growth (Cavalcanti et al., 2018; Gouveia *et al*., 2026). Although seed isotopic composition was unchanged, the reduced mass and pronounced depletion of storage-associated fatty acids indicate an effect on reserve allocation rather than on overall elemental balance. Notably, the ability of exogenous sucrose to normalize establishment in *dapat* seedlings (Extended Data Fig. 3a,b) further supports the idea that the mutant's early growth defect reflects an insufficient endogenous carbon supply during the transition to autotrophy.

In this context, the vegetative phenotype likely results from a metabolic imbalance that starts with altered seed reserve composition and continues as a pre-stress state during post-germinative growth. Building on the seed phenotype and storage composition findings, we found that the DAPAT mutation causes coordinated defects in vegetative growth (Extended Data Fig. 5a) and reproductive progression, including reduced leaf expansion and rosette growth, delayed inflorescence initiation, altered flowering time, and branching patterns (Figs. 1–2).

Under LD conditions, *dapat* plants exhibited delayed bolting (T_{50}: 6.75 versus 4 days in WT; Fig. 3a), whereas under ND conditions the phenotype was reversed, with accelerated flowering (T_{50}: 9.92 versus 12.33 days in WT; Fig. 3b). These results indicate that DAPAT-dependent metabolism interfaces with circadian and photoperiodic regulation to control flowering-time establishment (Maple *et al*., 2024). The LD-grown reveled *dapat* plants production of fewer primary rosette branches (R1; Fig. 2b) and primary cauline branches (C1; Fig. 2d), without altering secondary branches (R2; Fig. 2c; C2; Fig. 2e), indicating restricted primary bud outgrowth and coordination between flowering-time regulation and C1 emergence (Fichtner et al., 2022). Following the photoperiod switch, ND conditions reallocate branching toward rosettes in *dapat*: secondary cauline branches decrease (C2; Extended Data Fig. 2f), the R1/RL ratio rises (Extended Data Fig. 2j), and primary rosette branches increase (R1; Extended Data Fig. 2c), while primary cauline (C1; Extended Data Fig. 2e) and secondary rosette (R2; Extended Data Fig. 2b) branches remain unchanged. This ND-specific reinforcement of R1 suggests that DAPAT deficiency redirects resources to rosette branching in the absence of long-days signals.

Photoperiod-dependent CO/FLC regulation: DAPAT mutation amplifies floral repression despite elevated CO

To extend our analysis of *dapat* development and the photoperiod-dependent variation in shoot branching, we next examined the transcript levels of key flowering-time genes. Prior to bolting, *dapat* plants exhibit elevated *CO* and *FLC* expression, reduced *FRI*, and unchanged *FT* transcript levels (Fig. 4a,b). This pattern indicates that lysine deficiency strengthens FLC-mediated floral repression despite enhanced *CO* expression (Hepworth *et al*., 2002, Jiang et al., 2008). The reduced *FRI* levels contrast with its typical role in *FLC* upregulation via chromatin remodeling (Choi et al., 2011), suggesting alternative mechanisms drive *FLC* expression in *dapat* mutant. The elevated *CO* expression likely represents feedback to delayed flowering, as *CO* is regulated by circadian and photoperiodic cues (Valverde *et al*., 2008; Shim *et al*., 2016). However, *FLC*-mediated repression appears sufficient to suppress *CO* upregulation, preventing *FT* induction and maintaining floral suppression, thereby demonstrating the hierarchical dominance of *FLC* in flowering control. To probe these, we assessed the expression levels of genes encoding histone H3K9 methyltransferases of the Suppressor of variegation 3–9 homolog (SUVH) family, which are known to deposit repressive marks at flowering loci (Liu et al., 2010). Enhanced *SUVH4* (also named *KYP*) alongside reduced *SUVH5* expression (Fig. 5d) suggests remodeling of H3K9 landscapes (Rajakumara et al., 2011; Yu et al., 2017) to reinforce *FLC* repression (Liu et al., 2010). Furthermore, the leaf morphology of *dapat* mutants reveals notable alterations, including reduced leaf number and pronounced leaf curling (Extended Data Fig. 5b,c), resembling *kyp* and

kyp/suvh5/6 mutants and their interactions with the histone deacetylase 6 (HDA6; EC 3.5.1.98). Higher order *hda6*, *kyp*, and *suvh5/6* combinations produce sharply curled, serrated, and smaller leaves, underscoring the role of epigenetic module in leaf morphogenesis (Hung et al., 2023).

Lysine-biosynthesis disruption remodels DNA methylation landscapes

Epigenetic mechanisms are central to flowering time regulation, integrating environmental signals via chromatin modifications (He et al., 2019; Zhao et al., 2022; Roelfs et al., 2024). Considering the interplay between lysine metabolism, *S*-adenosylmethionine (SAM) availability (Hacham et al., 2007) and histone methylation landscapes (Guo, et al., 2010; Yan et al., 2019), we analyzed *S*-adenosylmethionine synthases (*MATs*) transcript levels (Fig. 5c,d). Elevated *MAT2* and *MAT4* expression (Fig. 5c) suggests altered SAM homeostasis in *dapat* plants. Among *Arabidopsis* MAT isoforms, MAT4 predominantly controls SAM production (Boerjan *et al*., 1990; Sekula *et al*., 2021), synthesizing SAM from methionine and ATP. Its loss in *mat4* knockouts depletes cellular SAM pools by ~ 35%, concomitantly reducing CHG/CHH DNA methylation and H3K9me2 levels (Meng et al., 2018; Yan et al., 2019). The upregulation of *MAT4* transcripts in *dapat* plants suggests elevated SAM levels in mutant tissues, consistent with the previously reported accumulation of methionine–SAM pathway enzymes in this genotype (Cavalcanti et al., 2018). This is further underscored by increased abundance of *S*-adenosylmethionine synthase 2 (AT4G01850), *S*-adenosylmethionine synthase 3 (AT2G36880), and methionine synthase 1 (AT5G17920) leaf proteins in the mutant, indicating coordinated rewiring of the methionine–SAM route. Together, these findings support an altered interplay between DAPAT-mediated lysine biosynthesis impairment and SAM availability in *dapat* plants, with implications for DNA methylation and flowering-time gene regulation (Meng et al., 2018; Yan et al., 2019).

Genome-wide methylome remodeling underlies metabolic–epigenetic coordination in the dapat mutant plants

Given the implications arising from the above experiments, methylome profiling proved essential, revealing that disruption of lysine biosynthesis in the *dapat* mutant induces widespread remodeling of the DNA methylation landscape, consistent with studies linking metabolic fluxes to epigenetic regulation (for review, *please see* Hayashi et al., 2023). We identified 749 CpG differentially methylated genes (DMGs) in *dapat* relative to WT (490 retained after 20% cutoff), which hierarchical clustering resolved into hyper- and hypomethylated clusters, mirroring reports that metabolic perturbations can trigger locus-specific methylation changes (Su et al., 2016; Meng et al., 2018; Lindermayr et al., 2020). In parallel, CHG and CHH-contexts bisulfite sequencing revealed 104 DMGs (104 CHG DMGs and 6 CHH DMGs retained after 20% cutoff), segregating similarly into hyper- and hypomethylated groups and mapping genome-wide with peaks on chromosomes 1 and 3 and 1 and 2 respectively (Fig. 6a-c); these distributions mirror findings that CHG methylation patterns are particularly sensitive to alterations in methyl donor availability (Yu *et al*., 2018).

To gain functional insight into the DMGs identified in *dapat* mutants, we performed GO enrichment analysis of biological processes, which highlighted cell morphogenesis, developmental growth involved

in morphogenesis, unidimensional cell growth, and cytoskeleton organization as the top-enriched categories (Fig. 7a). Locus-level inspection of the top-enriched categories revealed that most DMGs displayed moderate CpG hypomethylation at promoter regions, with comparatively smaller changes in CHG and CHH contexts (Fig. 7b-d). Within the cell morphogenesis category (n = 19 genes), the coherent CpG hypomethylation observed across the shared gene core (*BRI1*, *FEI1*, *ANX2*, *COBL7*, *RIC5*, *PAS1*, *XRN4* and *NMNAT*) may reflect a metabolic constraint on the aspartate-derived network: the DAP pathway constrain in the *dapat* mutant likely diverts the common precursor pool toward threonine synthesis, potentially limiting methionine flux (Galili, 2011) and, consequently, SAM availability.

Given that SAM is the sole methyl donor for MET1-mediated CpG maintenance, which could cause passive loss of CpG marks over successive cell divisions (Law & Jacobsen, 2010; Saze *et al*., 2003). This metabolic route to hypomethylation is conceptually analogous to epigenetic reprogramming reported under phosphate and nitrogen starvation (Yong-Villalobos *et al*., 2016; Mager & Ludewig, 2018). The resulting open chromatin at growth gene promoters might represent a compensatory epigenetic response attempting to upregulate cell expansion through *BRI1*-driven brassinosteroids signaling (Nolan *et al*., 2020), wall-integrity sensing via *FEI1* (Xu *et al*., 2008), polarity establishment by *RIC5* (Fu *et al*., 2005) and *ANX1/2* (Boisson-Dernier *et al*., 2009; Ge *et al*., 2017), and cellulose deposition via *COBL7* (Ge *et al*., 2024), yet likely insufficient to rescue the dwarf phenotype, as upstream metabolic limitations may prevail over the permissive chromatin state.

A largely similar distribution was observed for developmental growth involved in morphogenesis (n = 19 genes), where the same promoter-biased CpG hypomethylation pattern predominated and the targeted hypermethylation at *WAK2* and AT3G01015 suggests complementary adaptive logic. *WAK2* silencing might reflect active suppression of energy-costly wall surveillance (He *et al*., 1999), consistent with the constitutive defense-like state reported in *dapat* plants (Rate & Greenberg, 2001; Song et al., 2004). The tri-context hypermethylation at AT3G01015 likely reflects coordinated CMT3/H3K9me2- and RdDM-mediated heterochromatic silencing (Stroud *et al*., 2014; Fang et al., 2022; Zemach *et al*., 2013), possibly reinforced to insulate flanking morphogenetic loci from transposon reactivation under metabolic stress.

The context-specificity of these changes may reflect the differential sensitivity of methylation pathways to SAM availability, with MET1-dependent CpG maintenance more directly coupled to methyl donor flux than CMT3 or RdDM (Law & Jacobsen, 2010). Additionally, the recurrent presence of *XRN4* across all three GO terms (Fig. 7b-d) suggests that epigenetic reprogramming in the *dapat* mutant may be reinforced by post-transcriptional mRNA buffering (Souret *et al*., 2004). Collectively, genes such as *NMNAT*, *PAS1* (Vittorioso *et al*., 1998; Smyczynski *et al*., 2006) and *COBL7* (Ge *et al*., 2024) in the unidimensional cell growth category (n = 17 genes) illustrate that epigenetic access alone is likely insufficient for functional recovery when the required metabolic substrates (ATP, UDP-glucose, and specific biosynthetic precursors) cannot be adequately supplied. This interpretation is broadly consistent with the severe developmental defects observed upon total methylation loss in *Arabidopsis* (Liang et al., 2022) and suggests that metabolism, rather than epigenetic state, ultimately determines the phenotype. In line with this, repression of *CYT1* (CRY1/CRYPT1), a blue-light photoreceptor promoting flowering

through *CO* and *FT* activation under both short- and long-days conditions, likely reflects a downstream manifestation of this metabolic–epigenetic interplay. Its potential promoter hypermethylation (Fig. 7d) would be expected to delay the juvenile-to-reproductive transition and impair photomorphogenesis (Exner et al., 2010).

On the other hand, CHG and CHH contexts revealed distinct patterns of differential methylation across the genome (Extended Data Figs. 6 and 7). Comparing CpG methylation and CHG/CHH changes for genes associated with cytoskeleton organization, microtubule-based processes, protein folding, and cellular component or protein-complex disassembly, most loci exhibited moderate CpG methylation shifts accompanied by comparatively smaller changes in non-CG contexts (Extended Data Fig. Figure 6a–e).

Several genes involved in cytoskeleton dynamics and glucan biosynthesis displayed CpG hypermethylation predominantly in promoter regions, whereas others showed more heterogeneous patterns distributed across exonic and distal intergenic regions (Extended Data Fig. 6). A similar trend was observed for additional pathways linked to endoplasmic reticulum-associated degradation (ERAD), cell wall cellulose metabolism and biosynthesis, β-glucan biosynthesis, and aluminum stress response (Extended Data Fig. 7a–e). In these categories, differential methylation was frequently concentrated at promoters and largely driven by CpG variation, while CHG/CHH differences remained relatively modest.

In summary, locus-level analyses reveal that methylation changes in *dapat* plants preferentially affect CpG sites at regulatory regions of genes linked to cytoskeleton organization, cell wall metabolism, and stress-related pathways, with promoter hypomethylation dominating the CpG context, balanced hyper- and hypomethylation characterizing CHG changes, and comparatively fewer DMGs detected in the CHH context. However, transcriptional responses were variable, suggesting that hypomethylation alone is insufficient to drive consistent gene activation. Such imbalanced methylation dynamics may contribute to delayed flowering by disrupting the coordination between DNA methylation and canonical flowering-time regulatory networks.

Our results support a model in which disruption of lysine biosynthesis alters SAM-dependent methylation homeostasis, leading to chromosome-biased remodeling of CpG, CHG and CHH methylation (Fig. 7). This epigenetic reprogramming underscores the metabolic crosstalk between amino acid biosynthesis and chromatin architecture, where perturbations in lysine metabolism propagate through the methionine cycle to reshape the plant epigenome (Kumar & Rani, 2023). Future profiling of histone marks such as H3K9me2, H3K27me3, and H4K20me1, combined with analysis of histone crosstalk mechanisms, will help clarify how these epigenetic layers interact to regulate plant development (Nakamura et al., 2025) in *dapat* plants. Together, these findings position lysine biosynthesis as a critical node connecting metabolic flux, epigenetic regulation, and developmental plasticity, highlighting the systems-level constraints that limit lysine biofortification strategies (Singh *et al*., 2025) and emphasizing the need to consider metabolic-epigenetic integration in breeding programs for climate-resilient crops Kumar & Rani, 2023).

4. Conclusions

Our results revealed that disruption of lysine biosynthesis in the *dapat* mutant extends far beyond amino acid metabolism, influencing seed fatty acid composition, the vegetative-to-reproductive transition, shoot branching plasticity and genome-wide DNA methylation dynamics. These findings position the DAPAT enzymatic step as a key metabolic node integrating primary metabolism with epigenetic regulation of plant development. Loss of *L*,*L*-DAPAT activity triggers extensive remodeling of CpG and CHG methylation landscapes across all five chromosomes and alters developmental timing in a photoperiod-dependent manner. Together, these changes uncover a previously unrecognized role for lysine biosynthesis in coupling metabolic state to developmental transitions and reproductive output, establishing a mechanistic link between lysine metabolism, SAM-dependent methylation pathway and architectural plasticity in *Arabidopsis thaliana*. More broadly, they highlight how perturbations in primary metabolism can propagate through epigenetic regulatory networks to shape plant development, providing an avenue for manipulating metabolic–epigenetic interfaces to improve crop performance and resilience.

5. Methods

5.1. Plant growth conditions

Arabidopsis ecotype Col-0 the *dapat* mutant - a lysine biosynthesis-deficient line (Rate & Greenberg, 2001; Song et al., 2004; Hudson et al., 2006; Cavalcanti et al., 2018; Neves et al., 2024; Gouveia *et al*., 2026), were used in this study. *Arabidopsis* seeds were surface-sterilized by stirring in 1 mL of 80% (v/v) ethanol containing 0.05% (v/v) Tween 20 for 5 minutes, followed by a 5-minute wash in 100% ethanol. Residual ethanol was removed, and seeds were air-dried for 2 hours under sterile conditions. Sterilized seeds were grown on half-strength Murashige and Skoog (Murashige & Skoog, 1962) medium (pH 5.7) with sucrose supplemented 1% (w/v) and 0.8% (w/v) agar. Plates were sealed with micropore tape and stratified in darkness at 4°C for 72 hours to synchronize germination. Seeds were germinated and grown for 10 days under neutral-days conditions (ND, 12-h/12-h light-dark) photoperiod under 130 µmol m^{-2} s^{-1} light intensity, and 60% humidity. Seedlings were transferred to soil and grown at 20°C/18°C, under both ND and long-day (LD, 16-h/8-h light-dark) conditions for a complete characterization of the vegetative-to-reproductive transition phase and samples were taken in the middle of the light period.

5.2. Silique and seed phenotypes

Silique length and diameter were determined using a stereomicroscope. Six to eight siliques per plant were analyzed from eight plants per genotype. Siliques were photographed and measured, and silique length, diameter and seed number were determined. Total seed weight was also evaluated. Silique measurements were performed using ImageJ software. Seed germination dynamics were assessed at 0, 24, 36, 48, 60, 72 and 84 h and expressed as the percentage of plants with protruding radicles in each population.

5.3. Metabolite levels

Metabolite extraction was performed by the immediate addition of a specific methanolic extraction buffer to approximately 20 mg of dried, ground seeds. Total protein levels (Bradford, 1976) were measured using the insoluble fraction.

5.4. Elemental analyzer isotope ratio mass spectrometry (EA-IRMS)

After lyophilization, seeds were homogenized into a fine powder by grinding in liquid nitrogen, and 2 mg of material was used for δ13C and C/N ratio determination. Analyses were performed using an Isoprime 100 isotope ratio mass spectrometer coupled to an ISOTOPE cube elemental analyzer (Elementar, Hanau, Germany) according to Gowik et al. (2011).

5.5. Fatty acid methyl esters (FAMEs) analysis

Fatty acid methyl esters (FAMEs) were generated from seed tissue using acid-catalyzed transesterification as described by Browse et al. (1986). Ground frozen seed samples (10 mg) were suspended in 1 mL of 3 N HCl in methanol containing 20 µg of dodecanoic acid (C12:0) as an internal standard (Browse et al., 1986; Ichihara & Fukubayashi, 2010). Samples were heated at 90°C for 60 minutes to allow tissue breakdown and fatty acid esterification (Ichihara et al., 2016). Phase separation was achieved by adding 1 mL of hexane and 1 mL of 1% (w/v) sodium chloride solution, followed by centrifugation at 2000 g for 5 minutes to facilitate layer stratification (Dodds et al., 2005). The upper organic phase containing esterified fatty acids was collected and stored at − 20°C until analysis. Gas chromatographic separation and mass spectrometric identification were conducted using an Agilent 7890B system coupled to a 7200-series quadrupole time-of-flight mass spectrometer (Agilent Technologies, Santa Clara, CA, USA) (Kremser et al., 2022). Sample (1 µL) were injected in splitless mode onto a HP-5MS fused silica capillary column (30 m × 0.35 mm i.d., 0.25 µm film thickness, 5% phenyl-95% methyl polysiloxane stationary phase) with helium as carrier gas at 1 mL·min⁻¹ (International Olive Council, 2015). The temperature program included an initial isothermal hold at 70°C for 1 minute, followed by a multi-step ramp of 25°C·min⁻¹ to 170°C, then 3°C·min⁻¹ to 220°C, and finally 25°C·min⁻¹ to 300°C with a 5-minute hold, resulting in a total analytical runtime of 29.87 minutes (Fina et al., 2022). Mass spectrometric were acquired using electron impact ionization at 70 eV, with a source temperature of 200°C, scanning across m/z 60–800 at 20 Hz (Dodds et al., 2005). Compound identification required spectral library matching scores exceeding 770 against the NIST/EPA/NIH Mass Spectral Database, with additional confirmation by retention time comparison using certified standards (Sigma-Aldrich EC10A-1KT, Sigma-Aldrich, 2025). Quantitative analysis employed selected representative fragment ions for peak integration and area determination using Agilent MassHunter Qualitative software (Kenar et al., 2019).

5.6. Gene Expression Analysis

Whole rosettes from five individual plants were harvested before bolting, during the middle of the light period. Total RNA was extracted using the RNeasy Plant Mini Kit (Qiagen, Cat. No. 74904) with on-column DNase I treatment (RNase-free, New England Biolabs, Cat. No. M0303) to eliminate genomic DNA contamination. RNA concentration was determined using a NanoDrop OneC Microvolume UV-Vis Spectrophotometer (Thermo Fisher Scientific), with A260/A280 ratios > 2.0 and A260/A230 ratios > 1.8 as quality indicators. RNA integrity was verified by 1.5% agarose gel electrophoresis stained with GelRed (Biotium), confirming distinct 28S and 18S ribosomal RNA bands. First-strand cDNA was synthesized from the four highest-quality total RNA samples per genotype/treatment using the LunaScript RT SuperMix Kit (New England Biolabs, Cat. No. E3010) in 20 µL reactions (25°C for 2 min, 55°C for 10 min, and 95°C for 1 min). No-RT controls were included to confirm the absence of genomic DNA contamination. Quantitative PCR was performed using Luna Universal qPCR Master Mix (New England Biolabs, Cat. No. M3003) on a StepOnePlus Real-Time PCR System (Applied Biosystems). Cycling conditions were 95°C for 60 s, followed by 40 cycles of 95°C for 15 s and 60°C for 30 s, with melting curve analysis from 60°C to 95°C. Gene expression was calculated using the comparative CT method (ΔΔCT) with UBC9 and PP2A as reference genes, with primer efficiencies validated between 90–110% efficiency (R^2 >0.99). The primers used for RT-qPCR (Extended Data Table 2) were designed using the Primer3Plus web application (Untergasser *et al*., 2012). Three biological replicates per genotype/treatment were used, with expression levels shown as mean ± standard error of normalized 2^(-ΔΔCt).

5.7. Whole-genome bisulfite sequencing

Genomic DNA was extracted from three biological replicates of *Arabidopsis* wild-type (WT) and *dapat* mutant plants bisulfite-converted using the EZ DNA Methylation-Gold Kit (Zymo Research). Libraries were prepared with the Accel-NGS Methyl-Seq DNA Library Kit (Swift Biosciences) and paired-end sequencing (2 × 151 bp) was performed on the NovaSeq X platform (Macrogen Inc., Seoul, Republic of Korea). Raw read quality was assessed with FastQC v0.11.7 (Andrews *et al*., 2010), and adapter trimming and quality filtering were performed using Trim Galore v0.6.10 (Krueger, 2012), including removal of 18 bp Adaptase-derived tails and reads shorter than 20 bp. Trimmed reads were aligned to the TAIR10.1 reference genome using BSMAP v2.90 (Xi and Li, 2009); only uniquely mapped reads were retained and PCR duplicates were removed with SAMBAMBA v0.5.9 (Tarasov et al., 2015). Alignment statistics were evaluated with Qualimap 2.2 (Okonechnikov et al., 2016). Per-cytosine methylation ratios were extracted using the methyratio.py script within BSMAP and annotated by genomic feature and CpG island context using the UCSC Genome Browser table browser, with feature intersections computed via BEDTools v2 (Quinlan & Hall, 2010).

Differentially methylated cytosines were identified using a two-tier strategy: a permissive threshold of ≥ 10% absolute methylation difference was applied for genome-wide visualization (hierarchical clustering heatmaps), maximizing sensitivity across the full landscape of methylation variation (Wreczycka et al., 2017; Akalin et al., 2012); a stringent threshold of ≥ 20% was subsequently applied for DMR identification and gene ontology analyses, to exclude the stochastic epigenetic drift that dominates at lower effect

sizes in single WT comparator designs (Becker et al., 2011; Schmitz et al., 2011; van der Graaf et al., 2015; Akalin et al., 2012; Song et al., 2016; Crisp *et al*., 2018). Subsequently, the gene ontology analysis was performed using R (version 4.5.2) with the following packages: readr, dplyr, tidyr, ggplot2, ggrepel, stringr, clusterProfiler, org.At.tair.db, and patchwork. Data was loaded and cleaned: column names were trimmed, and rows with missing difference or geneId were removed. Enrichment analysis was conducted using clusterProfiler::enrichGO with the TAIR gene identifiers, the org.At.tair.db annotation package, and the Biological Process ontology. A raw p-value cutoff of 0.05 was applied (Fisher's exact test, no multiple testing correction).

5.8. Statistical analysis and experimental design

The experiment followed a completely randomized design. Plants were randomly arranged in white trays and watered regularly. All statistical comparisons between genotypes were conducted using Student's t-test, with p-values displayed on graphs or significance indicated by asterisks ($p < 0.05$).

References

1. Akalin, A. et al. methylKit: a comprehensive R package for the analysis of genome-wide DNA methylation profiles. Genome Biol 13, R87 (2012).
2. Amir, R. Current understanding of the factors regulating methionine content in vegetative tissues of higher plants. Amino Acids 39, 917–931 (2010).
3. Andrews, S. FastQC: a quality control tool for high throughput sequence data. Available at: http://www.bioinformatics.babraham.ac.uk/projects/fastqc/ (2010).
4. Angelovici, R., Fait, A., Fernie, A. R. & Galili, G. A seed high-lysine trait is negatively associated with the TCA cycle and slows down Arabidopsis seed germination. New Phytologist 189, 148–159 (2011).
5. Araújo, W. L. et al. Identification of the 2-hydroxyglutarate and isovaleryl-CoA dehydrogenases as alternative electron donors linking lysine catabolism to the electron transport chain of Arabidopsis mitochondria. The Plant Cell 22, 1549–1563 (2010).
6. Araújo, W. L., Tohge, T., Ishizaki, K., Leaver, C. J. & Fernie, A. R. Protein degradation: an alternative respiratory substrate for stressed plants. Trends in Plant Science 16, 489–498 (2011).
7. Arruda, P., Kemper, E. L., Papes, F. & Leite, A. Regulation of lysine catabolism in higher plants. Trends in Plant Science 5, 324–330 (2000).
8. Arruda P, Barreto P. Lysine Catabolism Through the Saccharopine Pathway: Enzymes and Intermediates Involved in Plant Responses to Abiotic and Biotic Stress. Front Plant Sci. May 21;11:587 (2020)
9. Azevedo, R. A., Lancien, M. & Lea, P. J. The aspartic acid metabolic pathway, an exciting and essential pathway in plants. Amino Acids 30, 143–162 (2006).
10. Becker, C. et al. Spontaneous epigenetic variation in the Arabidopsis thaliana methylome. Nature 480, 245–249 (2011).

11. Berdasco, M. et al. Promoter DNA Hypermethylation and Gene Repression in Undifferentiated Arabidopsis Cells. PLOS ONE 3, e3306 (2008).
12. Bernhardt, K., Wilkinson, S., Weber, A. P. M. & Linka, N. A peroxisomal carrier delivers NAD+ and contributes to optimal fatty acid degradation during storage oil mobilization. The Plant Journal 69, 1–13 (2012).
13. Boerjan, W., Bauw, G., Van Montagu, M. & Inzé, D. Distinct Phenotypes Generated by Overexpression and Suppression of S-Adenosyl-L-Methionine Synthetase Reveal Developmental Patterns of Gene Silencing in Tobacco. The Plant Cell 6, 1401–1414 (1994).
14. Brewer, P. B., Dun, E. A., Gui, R., Mason, M. G. & Beveridge, C. A. Strigolactone Inhibition of Branching Independent of Polar Auxin Transport. Plant Physiol 168, 1820–1829 (2015).
15. Browse, J., McCourt, P. J. & Somerville, C. R. Fatty acid composition of leaf lipids determined after combined digestion and fatty acid methyl ester formation from fresh tissue. Analytical Biochemistry 152, 141–145 (1986).
16. Cavalcanti, J. H. F. et al. An L,L-diaminopimelate aminotransferase mutation leads to metabolic shifts and growth inhibition in Arabidopsis. Journal of Experimental Botany 69, 5489–5506 (2018).
17. Choi, K. et al. The FRIGIDA Complex Activates Transcription of FLC, a Strong Flowering Repressor in Arabidopsis, by Recruiting Chromatin Modification Factors. The Plant Cell 23, 289–303 (2011).
18. Crisp, P. A. et al. Stable unmethylated DNA demarcates expressed genes and their cis-regulatory space in plant genomes. Proc. Natl. Acad. Sci. U.S.A. 117, 23991–24000 (2020).
19. Davis, S. J. Integrating hormones into the floral-transition pathway of Arabidopsis thaliana. Plant Cell & Environment 32, 1201–1210 (2009).
20. De Jong, M. et al. Natural variation in Arabidopsis shoot branching plasticity in response to nitrate supply affects fitness. PLoS Genet 15, e1008366 (2019).
21. De Los Reyes, P. et al. CONSTANS alters the circadian clock in Arabidopsis thaliana. Molecular Plant 17, 1204–1220 (2024).
22. De Mendoza, A. et al. Large-scale manipulation of promoter DNA methylation reveals context-specific transcriptional responses and stability. Genome Biol 23, 163 (2022).
23. Deleris, A. et al. Loss of the DNA Methyltransferase MET1 Induces H3K9 Hypermethylation at PcG Target Genes and Redistribution of H3K27 Trimethylation to Transposons in Arabidopsis thaliana. PLoS Genet 8, e1003062 (2012).
24. Dodds, E. D., McCoy, M. R., Rea, L. D. & Kennish, J. M. Gas chromatographic quantification of fatty acid methyl esters: Flame ionization detection vs. Electron impact mass spectrometry. Lipids 40, 419–428 (2005).
25. Dong, G., Ma, D.-P. & Li, J. The histone methyltransferase SDG8 regulates shoot branching in Arabidopsis. Biochemical and Biophysical Research Communications 373, 659–664 (2008).
26. Engqvist, M., Drincovich, M. F., Flügge, U.-I. & Maurino, V. G. Two D-2-hydroxy-acid dehydrogenases in Arabidopsis thaliana with catalytic capacities to participate in the last reactions of the methylglyoxal

and beta-oxidation pathways. Journal of Biological Chemistry 284, 25026–25037 (2009).

27. Exner, V. et al. A Gain-of-Function Mutation of Arabidopsis CRYPTOCHROME1 Promotes Flowering. Plant Physiology 154, 1633–1645 (2010).
28. Fang, J. et al. Mechanistic basis for maintenance of CHG DNA methylation in plants. Nat Commun 13, 3877 (2022).
29. Fichtner, F. et al. Plasticity of bud outgrowth varies at cauline and rosette nodes in Arabidopsis thaliana. Plant Physiology 188, 1586–1603 (2022).
30. Fina, A. et al. A high throughput method for fatty acid profiling using simultaneous microwave-assisted extraction and derivatization followed by reversed fill/flush flow modulation comprehensive multidimensional gas chromatography. Advances in Sample Preparation 4, 100039 (2022).
31. Fontecave M, Atta M, Mulliez E. S-adenosylmethionine: nothing goes to waste. Trends Biochem Sci. May;29(5):243-9 (2004).
32. Gallavotti, A. The role of auxin in shaping shoot architecture. Journal of Experimental Botany 64, 2593–2608 (2013).
33. Göbel, M. & Fichtner, F. Functions of sucrose and trehalose 6-phosphate in controlling plant development. Journal of Plant Physiology 291, 154140 (2023).
34. Gouveia, D. G., W. E. B.Barrios, A. O.Martins, et al. Lysine Biosynthesis Defines a Metabolic Checkpoint for Gibberellin-Mediated Growth in Arabidopsis thaliana. Plant, Cell & Environment0: e70525 (2026).
35. Gowik, U., Bräutigam, A., Weber, K. L., Weber, A. P. M. & Westhoff, P. Evolution of C4 Photosynthesis in the Genus Flaveria : How Many and Which Genes Does It Take to Make C4? The Plant Cell 23, 2087–2105 (2011).
36. Guo, L., Yu, Y., Law, J. A. & Zhang, X. SET DOMAIN GROUP2 is the major histone H3 lysine 4 trimethyltransferase in Arabidopsis. Proc. Natl. Acad. Sci. U.S.A. 107, 18557–18562 (2010).
37. Hacham, Y., Song, L.-H., Schuster, G. & Amir, R. Lysine enhances methionine content by modulating the expression of S-adenosylmethionine synthase. The Plant Journal 51, 850–861 (2007).
38. Hayashi, K., Alseekh, S. & Fernie, A. R. Genetic and epigenetic control of the plant metabolome. Proteomics 23, 2200104 (2023).
39. He, Y., Chen, T. & Zeng, X. Genetic and Epigenetic Understanding of the Seasonal Timing of Flowering. Plant Communications 1, 100008 (2019).
40. Hemenway, E. A. & Gehring, M. Epigenetic Regulation During Plant Development and the Capacity for Epigenetic Memory. Annual Review of Plant Biology 74, 87–109 (2023).
41. Hildebrandt, T. M. Synthesis versus degradation: directions of amino acid metabolism during Arabidopsis abiotic stress response. Plant Molecular Biology 98, 121–135 (2018).
42. Hildebrandt, T. M., Nunes Nesi, A., Araújo, W. L. & Braun, H.-P. Amino Acid Catabolism in Plants. Molecular Plant 8, 1563–1579 (2015).

43. Hudson, A. O., Singh, B. K., Leustek, T. & Gilvarg, C. An LL-Diaminopimelate Aminotransferase Defines a Novel Variant of the Lysine Biosynthesis Pathway in Plants. Plant Physiology 140, 292–301 (2006).
44. Hung, F.-Y. et al. Arabidopsis histone H3 lysine 9 methyltransferases KYP/SUVH5/6 are involved in leaf development by interacting with AS1-AS2 to repress KNAT1 and KNAT2. Commun Biol 6, 219 (2023).
45. Ichihara, K. & Fukubayashi, Y. Preparation of fatty acid methyl esters for gas-liquid chromatography. Journal of Lipid Research 51, 635–640 (2010).
46. Ichihara, K. et al. Fatty acid analysis of triacylglycerols: Preparation of fatty acid methyl esters for gas chromatography. Analytical Biochemistry 495, 6–8 (2016).
47. Imaizumi, T. Arabidopsis circadian clock and photoperiodism: time to think about location. Current Opinion in Plant Biology 13, 83–89 (2010).
48. International Olive Council. Determination of fatty acid methyl esters by gas chromatography. (2015).
49. Janssen, B. J., Drummond, R. S. M. & Snowden, K. C. Regulation of axillary shoot development. Current Opinion in Plant Biology 17, 28–35 (2014).
50. Jiang, D., Wang, Y., Wang, Y. & He, Y. Repression of FLOWERING LOCUS C and FLOWERING LOCUS T by the Arabidopsis Polycomb Repressive Complex 2 Components. PLoS ONE 3, e3404 (2008).
51. Kaluscha, S. et al. Evidence that direct inhibition of transcription factor binding is the prevailing mode of gene and repeat repression by DNA methylation. Nat Genet 54, 1895–1906 (2022).
52. Kenar, A. et al. Electron Impact–Mass Spectrometry Fingerprinting and Chemometrics for Rapid Assessment of Authenticity of Edible Oils Based on Fatty Acid Profiling. Food Analytical Methods 12, 1322–1334 (2019).
53. Kremser, A., Jochmann, M. A. & Schmidt, T. C. Optimization and automation of rapid and selective analysis of fatty acid methyl esters in aqueous samples using SPME arrow-GC-MS/MS. Analytical and Bioanalytical Chemistry 414, 6287–6301 (2022).
54. Kumar M, Rani K. Epigenomics in stress tolerance of plants under the climate change. Mol Biol Rep. 2023 Jul;50(7):6201-6216. doi: 10.1007/s11033-023-08539-6. Epub 2023 Jun 9. PMID: 37294468.
55. Krueger, F. Trim Galore: a wrapper tool around Cutadapt and FastQC to consistently apply quality and adapter trimming to FastQ files. Available at: https://www.bioinformatics.babraham.ac.uk/projects/trim_galore/ (2012).
56. Lang, Z. et al. The Methyl-CpG-Binding Protein MBD7 Facilitates Active DNA Demethylation to Limit DNA Hyper-Methylation and Transcriptional Gene Silencing. Molecular Cell 57, 971–983 (2015).
57. Le H, Simmons CH, Zhong X. Functions and Mechanisms of Histone Modifications in Plants. Annu Rev Plant Biol. May;76(1):551-578 (2025).
58. Li, P., Wang, Z., Lu, Y. & Guo, Y. Phenotypic plasticity and stability in plants: Genetic mechanisms, environmental adaptation, evolutionary implications, and Future Directions. Plant, Cell &

Environment 48, 5847–5860 (2025).
59. Li, Q. et al. Regulation of Active DNA Demethylation by a Methyl-CpG-Binding Domain Protein in Arabidopsis thaliana. PLoS Genet 11, e1005210 (2015).
60. Li, X., Lin, C., Lan, C. & Tao, Z. Genetic and epigenetic basis of phytohormonal control of floral transition in plants. Journal of Experimental Botany 75, 4180–4194 (2024).
61. Liang, W. et al. Deciphering the synergistic and redundant roles of CG and non-CG DNA methylation in plant development and transposable element silencing. New Phytologist 233, 722–737 (2022).
62. Lindermayr, C., Rudolf, E. E., Durner, J. & Groth, M. Interactions between metabolism and chromatin in plant models. Molecular Metabolism 38, 100951 (2020).
63. Liu, C., Lu, F., Cui, X. & Wu, K. Histone Methylation in Higher Plants. Annual Review of Plant Biology 61, 395–420 (2010).
64. Luo, Z., Janssen, B. J. & Snowden, K. C. The molecular and genetic regulation of shoot branching. Plant Physiology 187, 1033–1044 (2021).
65. Mao, D. et al. FERONIA receptor kinase interacts with S-adenosylmethionine synthetase and suppresses S-adenosylmethionine production and ethylene biosynthesis in Arabidopsis. Plant, Cell & Environment 38, 2566–2574 (2015).
66. Mason, M. G., Ross, J. J., Babst, B. A., Wienclaw, B. N. & Beveridge, C. A. Sugar demand, not auxin, is the initial regulator of apical dominance. Proceedings of the National Academy of Sciences 111, 6092–6097 (2014).
67. Meng, J. et al. METHIONINE ADENOSYLTRANSFERASE4 Mediates DNA and Histone Methylation. Plant Physiology 177, 652–670 (2018).
68. Møller, B. L. Lysine Catabolism in Barley (Hordeum vulgare L.). Plant Physiology 57, 687–692 (1976).
69. Müller, D. & Leyser, O. Auxin, cytokinin and the control of shoot branching. Annals of Botany 107, 1203–1212 (2011).
70. Murashige, T. & Skoog, F. A Revised Medium for Rapid Growth and Bio Assays with Tobacco Tissue Cultures. Physiologia Plantarum 15, 473–497 (1962).
71. Nakamura K, Yamaguchi N, Ito T. The histone crosstalk code in plants: Deciphering epigenetic complexity. Curr Opin Plant Biol. Oct;87:102763 (2025).
72. Neves, T. G. et al. Lysine biosynthesis impairment gives cues about connection with TCA cycle intermediates in Arabidopsis response to salt disturbance. Theoretical and Experimental Plant Physiology 37, 6 (2024).
73. Okonechnikov, K., Conesa, A. & García-Alcalde, F. Qualimap 2: advanced multi-sample quality control for high-throughput sequencing data. Bioinformatics 32, 292–294 (2016).
74. Quinlan, A. R. & Hall, I. M. BEDTools: a flexible suite of utilities for comparing genomic features. Bioinformatics 26, 841–842 (2010).
75. Rajakumara, E. et al. A dual flip-out mechanism for 5mC recognition by the Arabidopsis SUVH5 SRA domain and its impact on DNA methylation and H3K9 dimethylation in vivo. Genes & Development

25, 137–152 (2011).

76. Rate, D. N. & Greenberg, J. T. The Arabidopsis aberrant growth and death2 mutant shows resistance to Pseudomonas syringae and reveals a role for NPR1 in suppressing hypersensitive cell death. The Plant Journal 27, 203–211 (2001).
77. Rébeillé, F. et al. Methionine catabolism in Arabidopsis cells is initiated by a γ-cleavage process and leads to S-methylcysteine and isoleucine syntheses. Proceedings of the National Academy of Sciences 103, 15687–15692 (2006).
78. Roelfs, K.-U., Känel, A., Twyman, R. M., Prüfer, D. & Schulze Gronover, C. Epigenetic variation in early and late flowering plants of the rubber-producing Russian dandelion Taraxacum koksaghyz provides insights into the regulation of flowering time. Sci Rep 14, 4283 (2024).
79. Schmitz, G. & Theres, K. Shoot and inflorescence branching. Current Opinion in Plant Biology 8, 506–511 (2005).
80. Schmitz, R. J. et al. Transgenerational Epigenetic Instability Is a Source of Novel Methylation Variants. Science 334, 369–373 (2011).
81. Sekuła, B., Ruszkowski, M. & Dauter, Z. S-adenosylmethionine synthases in plants: Structural characterization of type I and II isoenzymes from Arabidopsis thaliana and Medicago truncatula. International Journal of Biological Macromolecules 151, 554–565 (2020).
82. Shim, J. S., Kubota, A. & Imaizumi, T. Circadian Clock and Photoperiodic Flowering in Arabidopsis: CONSTANS Is a Hub for Signal Integration. Plant Physiology 173, 5–15 (2017).
83. Sigma-Aldrich. FAME Standard for Optimizing GC System Performance. (2025).
84. Singh V, Mishra M, Singla-Pareek SL, Roy JK, Pareek A. Lysine Matters: Genetic and Biotechnological Innovations to Combat Protein Malnutrition. Plant Cell Environ. Mar;49(3):1509-1529 (2026).
85. Song, J. T., Lu, H. & Greenberg, J. T. Divergent Roles in Arabidopsis thaliana Development and Defense of Two Homologous Genes, aberrant growth and death2 and AGD2-LIKE DEFENSE RESPONSE PROTEIN1, Encoding Novel Aminotransferases. The Plant Cell 16, 353–366 (2004).
86. Song, J., Zynda, G., Beck, S., Springer, N. M. & Vaughn, M. W. Bisulfite Sequence Analyses Using CyVerse Discovery Environment: From Mapping to DMGs. CP Plant Biology 1, 510–529 (2016).
87. Su, X., Wellen, K. E. & Rabinowitz, J. D. Metabolic control of methylation and acetylation. Current Opinion in Chemical Biology 30, 52–60 (2016).
88. Tarasov, A., Vilella, A. J., Cuppen, E., Nijman, I. J. & Prins, P. Sambamba: fast processing of NGS alignment formats. Bioinformatics 31, 2032–2034 (2015).
89. Valverde, F. et al. Photoreceptor regulation of CONSTANS protein in photoperiodic flowering. Science 303, 1003–1006 (2004).
90. Valverde, F. et al. Photoreceptor Regulation of CONSTANS Protein in Photoperiodic Flowering. Science 303, 1003–1006 (2004).
91. Van Der Graaf, A. et al. Rate, spectrum, and evolutionary dynamics of spontaneous epimutations. Proc. Natl. Acad. Sci. U.S.A. 112, 6676–6681 (2015).

92. Wahl, V. et al. Regulation of flowering by trehalose-6-phosphate signaling in Arabidopsis thaliana. Science 339, 704–707 (2013).
93. Wang, B., Smith, S. M. & Li, J. Genetic Regulation of Shoot Architecture. Annual Review of Plant Biology 69, 437–468 (2018).
94. Wang, F., Han, T. & Chen, Z. J. Circadian and photoperiodic regulation of the vegetative to reproductive transition in plants. Communications Biology 7, 579 (2024).
95. Wang, Y. & Jiao, Y. Axillary meristem initiation-a way to branch out. Current Opinion in Plant Biology 41, 61–66 (2018).
96. Wreczycka, K. et al. Strategies for analyzing bisulfite sequencing data. Journal of Biotechnology 261, 105–115 (2017).
97. Xi, Y. & Li, W. BSMAP: whole genome bisulfite sequence MAPping program. BMC Bioinformatics 10, 232 (2009).
98. Yan, X. et al. METHIONINE SYNTHASE1 Is Involved in Chromatin Silencing by Maintaining DNA and Histone Methylation. Plant Physiology 181, 249–261 (2019).
99. Yang, Q., Zhao, D.-X. & Liu, Q. Connections Between Amino Acid Metabolisms in Plants: Lysine as an Example. Frontiers in Plant Science 11, 928 (2020).
100. Yu, C.-W. et al. HISTONE DEACETYLASE6 Acts in Concert with Histone Methyltransferases SUVH4, SUVH5, and SUVH6 to Regulate Transposon Silencing. The Plant Cell 29, 1970–1983 (2017).
101. Zhang, R. et al. SNP Cutter: a comprehensive tool for SNP PCR-RFLP assay design. Nucleic Acids Research 33, W489–W492 (2005).
102. Zhao, L. et al. DNA methylation underpins the epigenomic landscape regulating genome transcription in Arabidopsis. Genome Biology 23, 197 (2022).
103. Zhu, X. & Galili, G. Lysine Metabolism Is Concurrently Regulated by Synthesis and Catabolism in Both Reproductive and Vegetative Tissues. Plant Physiology 135, 129–136 (2004).

Figures

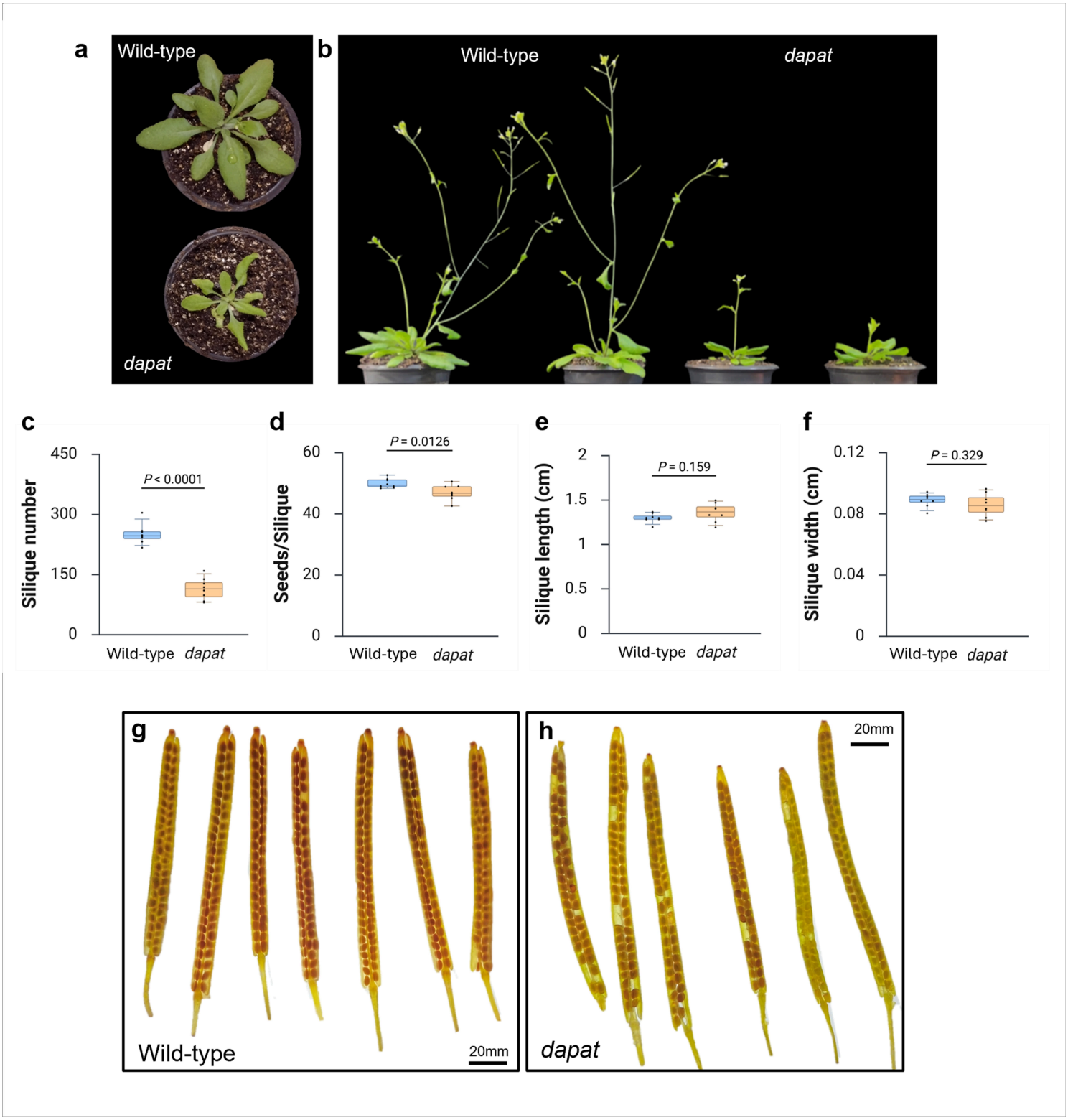


Figure 1

Lysine biosynthesis deficiency alters vegetative growth and reproductive output in *Arabidopsis thaliana* under long-days. a.Phenotype of four-week-old *Arabidopsis* wild-type (WT) and *dapat* mutant plants grown under a 16-h light photoperiod (long-days), 20 °C day/18 °C night, and 150 µmol m^{-2} s^{-1} light intensity. **b.** Phenotype during the reproductive phase transition of five-week-old *Arabidopsis* WT and *dapat* plants under long-days photoperiod. **c.** Total number of siliques per plant. **d.** Seeds per silique.

e.Silique length. **f.** Silique width. Data are presented as mean ± SEM (n = 8). Statistical comparisons were performed using one-way ANOVA followed by Tukey's HSD test (α = 0.05). **g-h.** Mature siliques of eight-week-old *Arabidopsis*WT and *dapat* mutant.

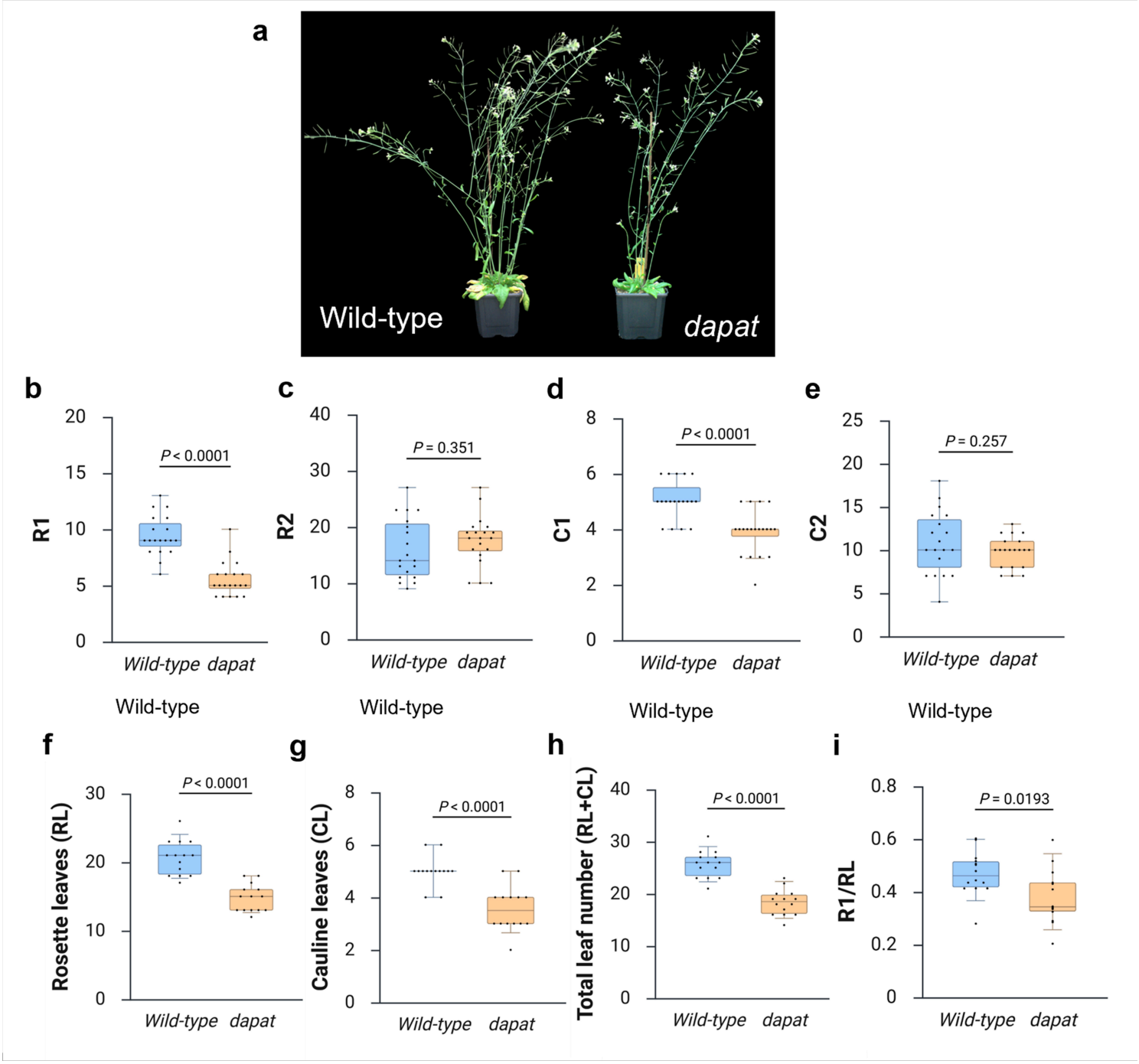


Figure 2

Modified shoot branching and leaf production in lysine-deficient *Arabidopsis* mutant. a. *Arabidopsis* wild-type (WT) and *dapat* mutant plants during the reproductive phase transition under 16-h light photoperiod (long-days), at 20°C during the day and 18°C at night, with a light intensity of 150 µmol $m^{-2}s^{-1}$. **b.** Primary rosette branches (R1). **c.** Secondary rosette branches (R2). **d.** Primary cauline branches (C1). **e.** Secondary cauline branches (C2). Data are presented as mean ± SEM (n = 14). **f.**

Number of rosette leaves (RL). **g.** Number of cauline leaves (CL). **h.** Total leaf count. **i.** Ratio of primary rosette branches (R1) to rosette leaves (RL). Different letters denote statistically significant differences between genotypes (one-way ANOVA followed by Tukey's HSD test, α = 0.05).

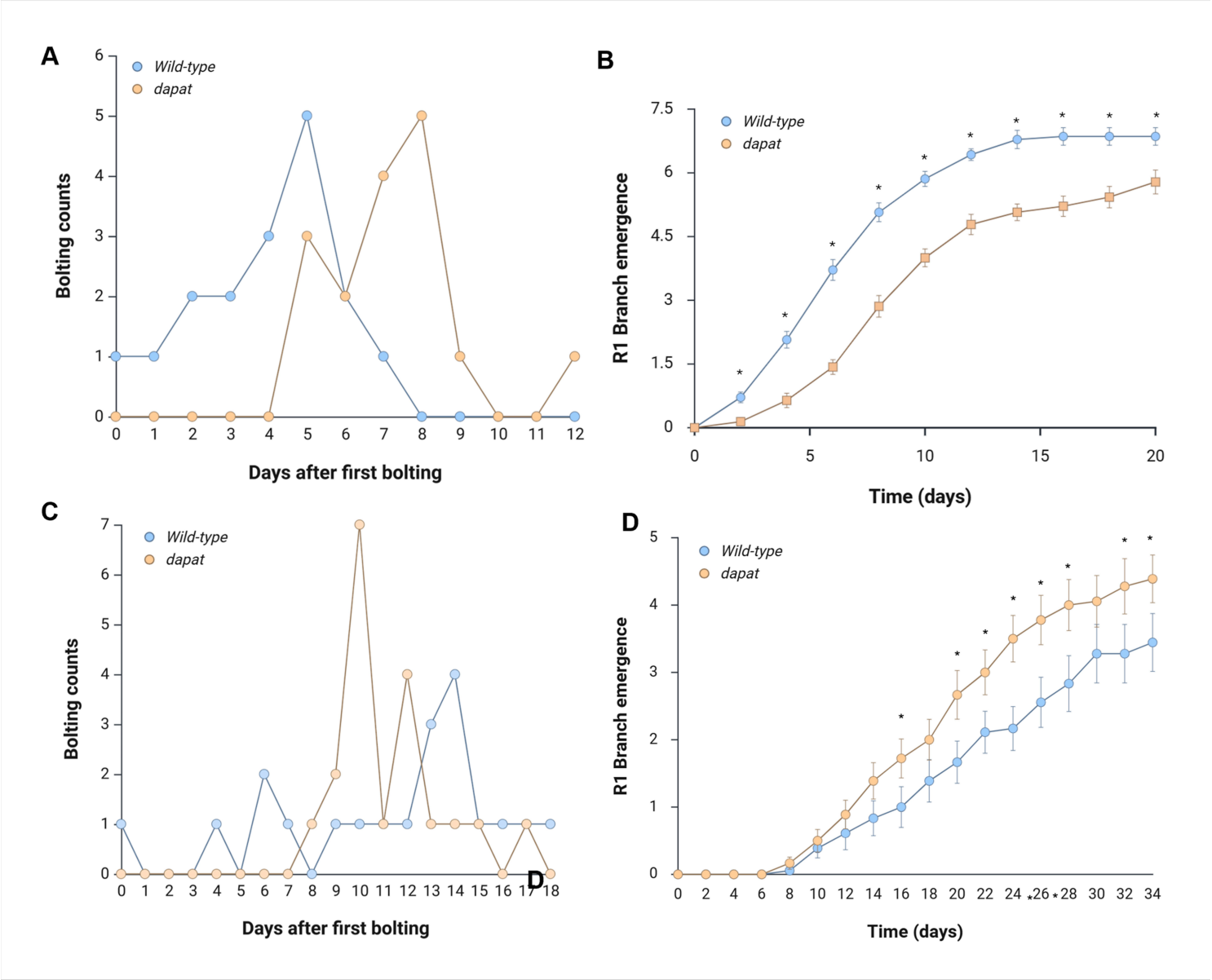


Figure 3

Defective lysine synthesis alters bolting time and primary rosette branching under distinct photoperiods. Bolting timeline, where bolting is defined as the day the main stem elongates beyond 0.5 cm. Here, "days to bolting" represent the interval from sowing under light conditions to bolting. **a.** *Arabidopsis* wild-type (WT) and *dapat* mutant plants under a 16-h light photoperiod (long-days), 20 °C day/18 °C night, and 150 µmol m^{-2} s^{-1} light intensity. **b.**Primary rosette branches (R1) per plant counted every two days after bolting under long-days. Branches ≥ 0.5 cm were scored. Asterisks denote values significantly different from WT (Student's t-test, P < 0.05). Data are mean ± SEM (n = 14). **c.** WT and *dapat* mutant plants under a 12-h photoperiod (neutral-days). **d.** Primary rosette branches (R1) per plant

counted every 2 days after bolting in plants grown under neutral-days. Branches ≥ 0.5 cm were scored. Asterisks denote values significantly different from WT (Student's t-test, P < 0.05). Data are mean ± SEM (n = 18).

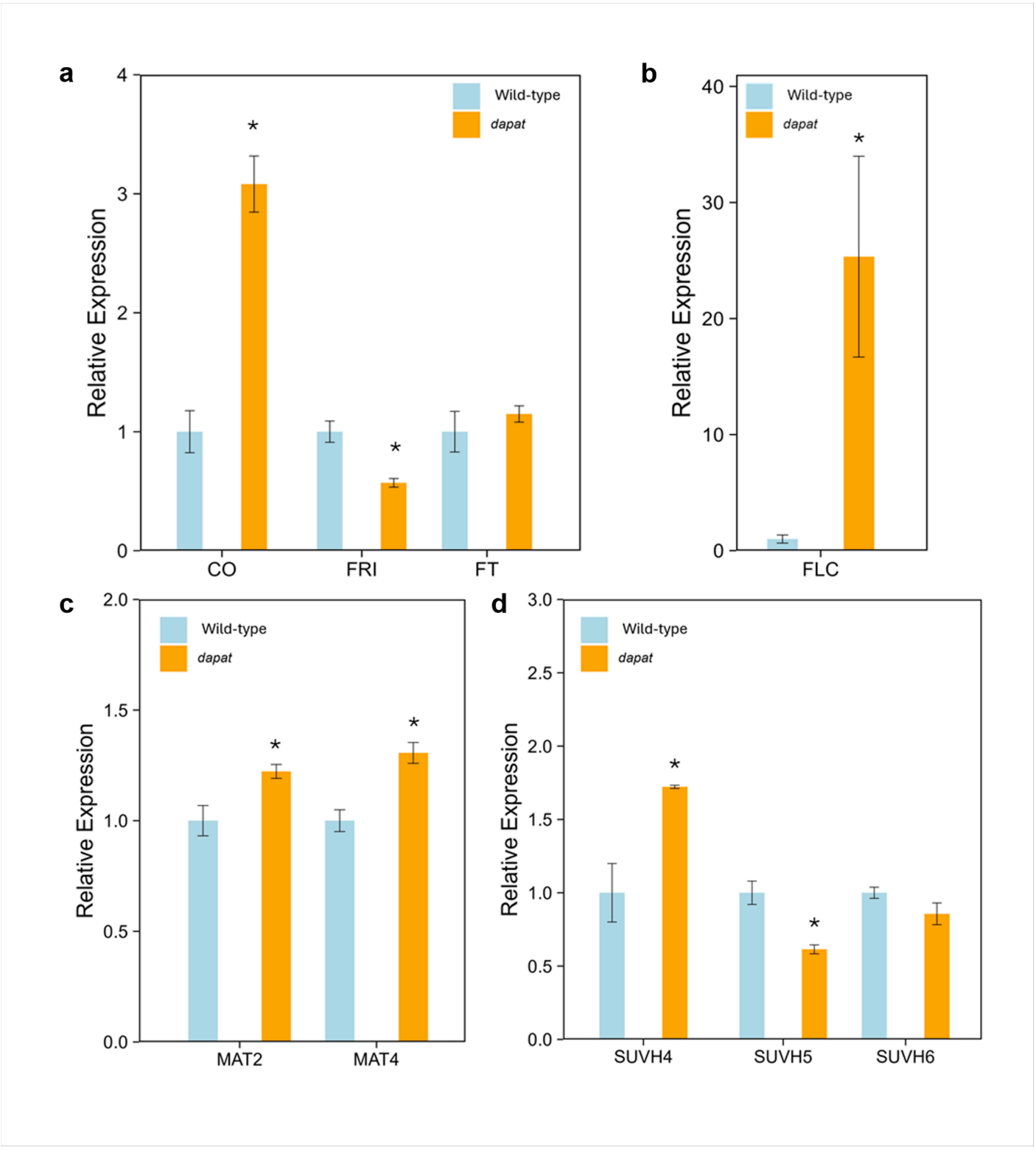


Figure 4

DAPAT mutation alters flowering-time gene expression and chromatin-modifying enzyme transcripts. **a.** Expression of flowering regulators *CO*(AT5G15840), *FRI* (AT4G00650) and *FT* (AT1G65480). **b.** *FLC*(AT5G10140) transcript levels. **c.** *S*-adenosylmethionine synthase *MAT2*(AT4G01850) and *MAT4* (AT3G17390). **d.** Histone methyltransferases *SUVH4*(AT5G13960), *SUHV5* (AT2G35160) and *SUVH6* (AT2G22740). RNA was extracted from 4-week-old pre-bolting *Arabidopsis* wild-type (WT) and *dapat*mutant plants grown under a 12-h light photoperiod (neutral-days), sampled mid-light period. Asterisks denote significant differences from WT (Student's t-test, P < 0.05). Data: mean ± SEM (n = 3).

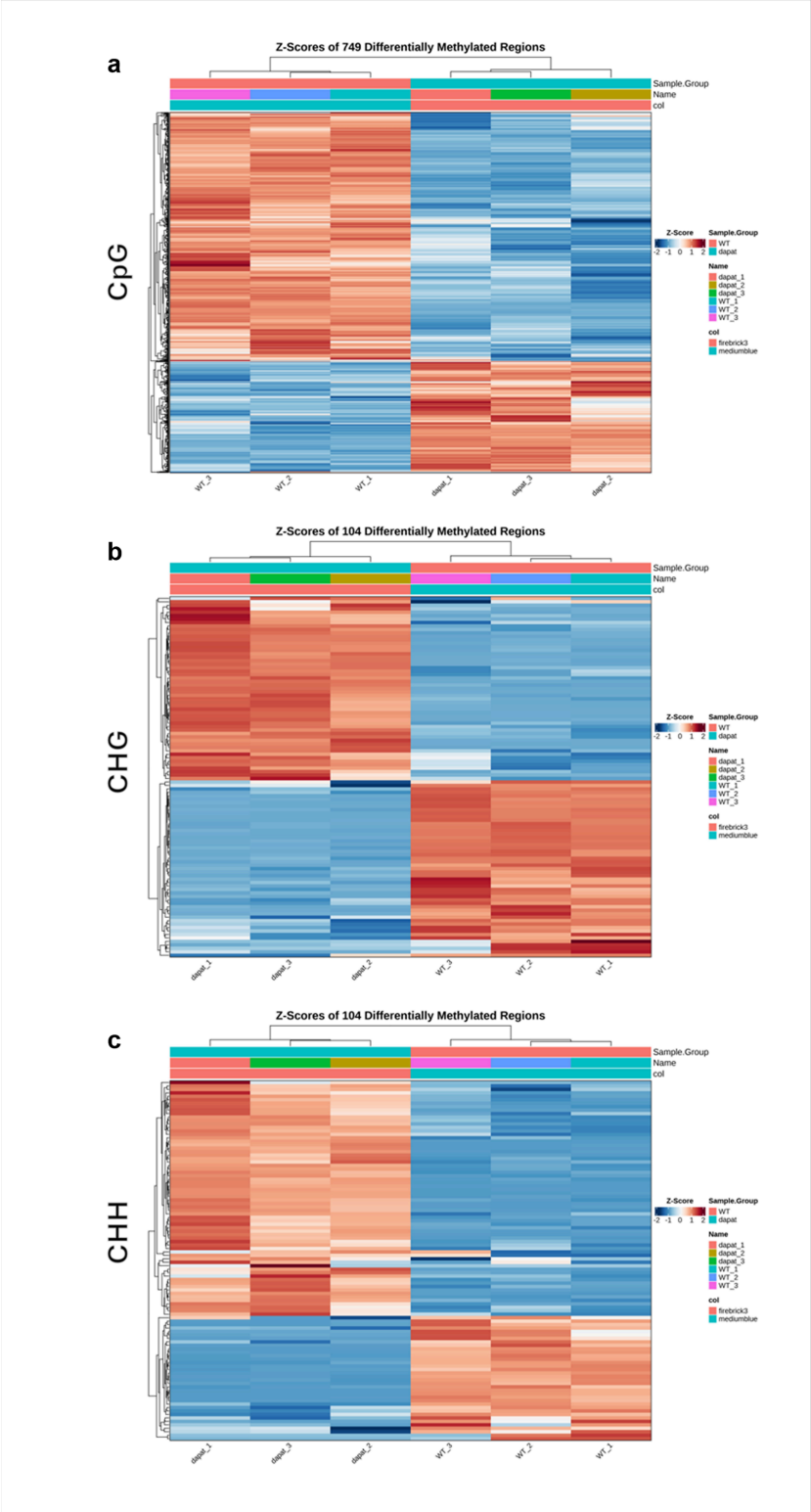


Figure 5

Epigenome-wide methylation landscape and differentially methylated genes (DMGs) analysis at CpG, CHG and CHH contexts. Heatmap of Z-scores for **a.** 749 CpG. **b.** 104 CHG. **c.**104 CHH differentially methylated 200 bp tiles between *Arabidopsis*wild-type (WT) and *dapat* mutant plants. Z-scores represent row-centered methylation levels, with blue indicating hypomethylation and red indicating hypermethylation. Columns correspond to three biological replicates for each genotype as indicated by the top and bottom annotation bars. Rows (tiles) are ordered by hierarchical clustering (left dendrogram), revealing distinct hyper- and hypomethylation blocks that differentiate the two genotypes.

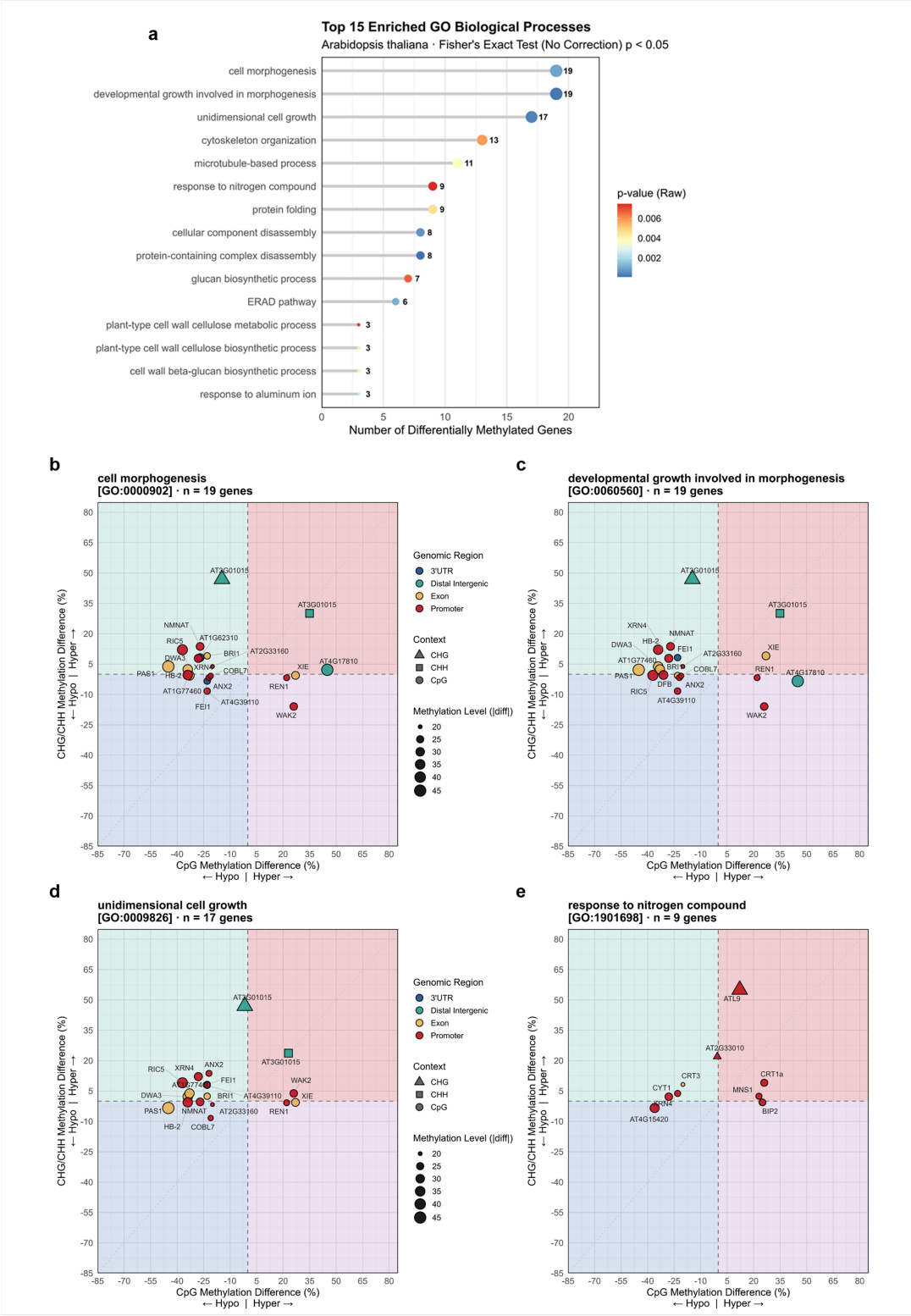


Figure 6

DNA methylation changes associated with enriched biological processes in *dapat* mutant plants. a. Gene Ontology (GO) Biological Process enrichment analysis of differentially methylated genes (DMGs) identified between *Arabidopsis* wild-type (WT) and *dapat* mutant plants. The top 15 enriched terms (by p-value) are shown, ordered by gene count. **b–e.** Genome-wide scatter plots of differentially methylated genes (DMGs) from selected enriched GO categories: **b.**cell morphogenesis (GO:0000902; n = 19), **c.**

developmental growth involved in morphogenesis (GO:0060560; n = 19), **d.** unidimensional cell growth (GO:0009826; n = 17), and **e.** response to nitrogen compound (GO:1901698; n = 9). Axes show CpG methylation difference (%) versus CHG or CHH difference (%), with negative and positive values indicating hypo- and hypermethylation in *dapat* relative to WT. Each point represents a DMG (|Δmethylation| ≥ 20%). Point shape indicates cytosine context (circles, CpG; squares, CHH; triangles, CHG), color indicates genomic feature (promoter, exon, distal intergenic, or 3'UTR), and size reflects the magnitude of methylation difference. Selected loci are labelled.

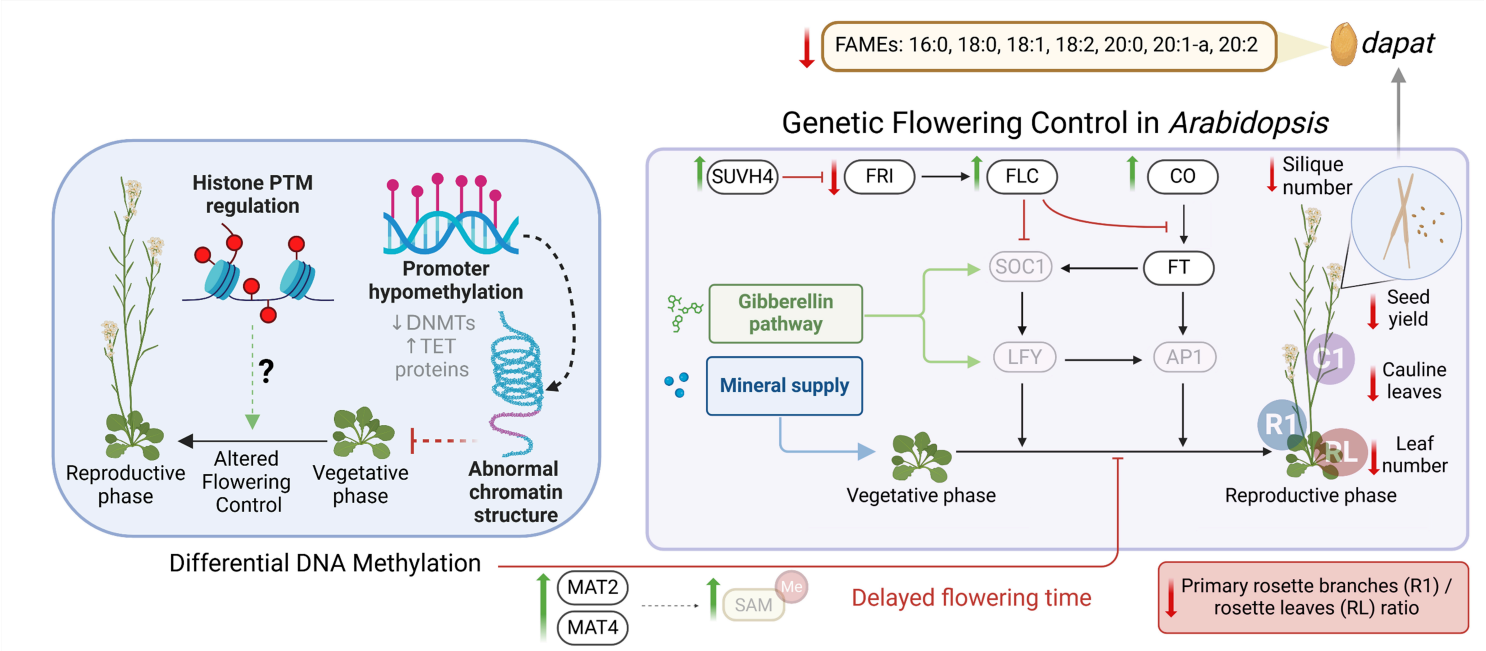


Figure 7

Overview of regulatory disturbances associated with the DAPAT mutation. Impaired lysine biosynthesis at the DAPAT (*L,L*-diaminopimelate aminotransferase) step in *dapat* is associated with depletion of fatty acid methyl esters (FAMEs) 16:0, 18:0, 18:1, 18:2, 20:0, 20:1-a and 20:2, suggesting a metabolic shift that may contribute to defects in development and flowering initiation. These alterations coincide with changes in secondary branching patterns and with widespread DNA methylation reprogramming, including promoter hypomethylation, and may further impinge on histone-related chromatin regulation. Opaque gene symbols indicate loci directly measured in this study by RT-qPCR, whereas transparent elements represent pathway components included for context. Dashed arrows and question marks denote hypothetical links that require further validation. *Abbreviations:* MAT2, *S*-adenosylmethionine synthetase 2; MAT4, *S*-adenosylmethionine synthetase 2; SAM, *S*-adenosylmethionine; SUVH4, suppressor of variegation 3-9 homolog 4; FRI, FRIGIDA; FLC, FLOWERING LOCUS C; CO, CONSTANS; SOC1, SUPPRESSOR OF OVEREXPRESSION OF CONSTANS 1; LFY, LEAFY; FT, FLOWERING LOCUS T; AP1, APETALA1; C1, cauline primary branches; R1, primary rosette branches; RL, rosette leaves; PTM, post-translational modification; DNMTs, DNA methyltransferases; TET proteins, ten-eleven translocation proteins.

Supplementary Files

This is a list of supplementary files associated with this preprint. Click to download.

- SupplementaryTable2.docx
- ExtendedDataFig.2.png
- SupplementaryTable1.docx
- ExtendedDataFig.5.png
- ExtendedDataFig.4.tif
- SupplementaryTable3.xlsx
- ExtendedDataFig.1.png
- ExtendedDataFig.8.tif
- ExtendedDataFig.7.tif
- ExtendedDataFig.6.tif
- ExtendedDataFig.3.tif
- ExtendedDataTableLegends.docx